

U.S. DEPARTMENT OF COMMERCE
NATIONAL OCEANIC AND ATMOSPHERIC ADMINISTRATION
NATIONAL WEATHER SERVICE
NATIONAL METEOROLOGICAL CENTER

OFFICE NOTE 325

UTILIZATION OF SATELLITE RADIATIVE IMAGERY
DATA FOR IMPROVEMENT IN THE ANALYSIS OF
DIVERGENT WIND IN THE TROPICS

AKIRA KASAHARA
UCAR VISITING SCIENTISTS
DEVELOPMENT DIVISION

RAMESH C. BALGOVIND
BERT B. KATZ

UCAR PROGRAMMING STAFF
SIGMA DATA SERVICES CORPORATION
DEVELOPMENT DIVISION

DECEMBER 1986

THIS IS AN UNREVIEWED MANUSCRIPT, PRIMARILY INTENDED FOR
INFORMAL EXCHANGE OF INFORMATION AMONG NMC STAFF MEMBERS.

ABSTRACT

A scheme is proposed to incorporate satellite radiative imagery data into the specification of initial conditions for the NMC operational global prediction model in order to improve the analysis of divergent wind field in the tropics. The basic assumptions are that outgoing longwave radiation (OLR) data can provide (1) the division between convective (upward motion) and clear sky (downward motion) areas, and (2) the height of convection cells. The intensity of ascending motion in the convective areas is estimated based on OLR data. The intensity of descending motion is evaluated from the thermodynamic energy balance between radiative cooling and adiabatic warming, since the local time change of temperature is small in the tropics. Once the vertical motion field is determined, the horizontal divergence field can be calculated from the mass continuity equation. Then, the divergent part of wind is determined. The proposed scheme is tested using the NMC analysis data set of January 21, 1985, with satisfactory results.

I. INTRODUCTION

During the very first hours of a forecast run, the amount of condensed water and, consequently, the amount of released latent heat are usually too small, particularly in the tropics. This spin-up problem appears in all forecast models, including operational ones (Girard and Jarraud, 1982; Heckley, 1985.) It is one of the most serious problems in numerical weather prediction. This problem may be caused by inaccuracies in the initial specification of divergence, moisture and thermal fields, and/or due to shortcomings in the parameterization of physical processes.

Although diabatic nonlinear normal mode initialization (NNMI) schemes are now employed at operational forecasting centers (e.g. Wergen, 1983), the initial specification of the divergence field appears to remain unsatisfactory due to deficiencies in the specification of diabatic heating rates which are used in the NNMI. This observation is born out of a recent work by Mohanty et al. (1986) in which several initialization schemes, including diabatic NNMI methods, were tested to examine which schemes can retain most of the analyzed divergence intensities after initialization. It was shown that the use of diabatic NNMI with model-generated heating rates (as practiced by many operational centers) retains far less intensity of analyzed divergence than does the use of diabatic NNMI with diagnosed heating rates. The diagnosed heating rates were determined as a residual of the thermodynamic energy balance using analyzed synoptic data. Consequently, employing this kind of diabatic heating is not applicable to operational forecasting, since the determination of heating requires prior knowledge of the predicted fields.

Therefore, it is clearly necessary to make use of more accurate diabatic heating rates in conjunction with the application of NNMI to obtain

a more reliable initial divergence field. One might suggest that the prediction model could generate adequate diabatic heating rates, if it were run on a continuous data assimilation mode (instead of traditional intermittent analysis procedures), because the problem of spin-up may not be present in a model with a continuous data assimilation mode. This suggestion, however, seems not totally workable in view of the present state of sophistication in the formulation of model physics. While radiative parameterizations produce accurate estimates of solar and infrared radiative fluxes under clear sky conditions, uncertainties exist when cloud effects are taken into account (since the cloud calculations are generally inaccurate). More uncertainties may exist in the evaluation of the latent heat of condensation through cumulus parameterizations. It is, therefore, desirable to develop a method of estimating the diabatic heating based on other independent data sources such as radiative imagery data from satellites and rainfall measurements. Krishnamurti et al. (1983) describe a procedure for the estimation of rainfall rates from a mix of satellite and rain gauge observations. Rainfall rates may be used to estimate the release of latent heat in convective regions.

With the specification of accurate diabatic heating rates, the application of diabatic NNMI will create a tropical divergent circulation. However, the question still remains as to whether or not the tropical divergent circulation thus created meets our need for an accurate initial divergence field. On one hand, the legitimacy of Machenhauer balance (even with diabatic effects) has been questioned in the tropics (Errico, 1984; Errico and Rasch, 1986). On the other hand, the application of diabatic NNMI does not necessarily provide a set of initial conditions

free from spin-up problems. As shown by Donner (1986), an additional initialization step must be performed to modify the moisture and temperature fields in order to initiate cumulus convection which releases the latent heat of condensation expected under a given divergence field. The need of data initialization for physical processes (cumulus convection in particular) in addition to data initialization for dynamical variables (such as mass and velocity fields) has begun to be recognized recently as a means to solve the spin-up problem (e.g. Krishnamurti et al., 1984).

The objective analysis of mass divergence or the irrotational part of velocity has been notoriously difficult because of its small magnitude compared with the rotational part of velocity. In fact, the irrotational part of velocity had been intentionally suppressed in the analysis of wind at the National Meteorological Center by means of the Hough analysis scheme (Flattery, 1977) until a new data assimilation scheme based on optimum interpolation (McPherson, et al., 1979) was introduced in preparation for the Global Weather Experiment (GWE) in 1979. The observational efforts of GWE were unprecedented in the degree of their global coverage. The availability of FGGE Level III analyses produced by the NMC, ECMWF, GFDL and GLA has made it attractive to examine the question of reliability in the mass divergence field. Many investigators (e.g. Krishnamurti and Ramanathan, 1982; Paegle and Baker, 1982; Murakami and Ding, 1982; and Lorenc, 1984) feel that the large-scale divergence field in the tropics contains significantly more usable information than previously believed observable. However, the question has been raised concerning the accuracy of the analyzed divergent wind field on a daily basis. For example, Julian (1985) indicates that a significant disparity exists between the

divergent wind analyses produced by the various centers, for scales smaller than approximately zonal wavenumber 10.

Kasahara et al. (1986) investigated the question of reliability in the analysis of tropospheric mean vertical motion field on a daily basis in conjunction with the evaluation of global diabatic heating rates using the ECMWF Level III b analyses. As a measure of verification, infrared and visible radiometric imagery data from the TIROS N polar-orbiting satellite are compared with the distributions of diabatic heating and vertical velocity. Satellite radiometric data have been used by many investigators to estimate rainfall rates in the tropics (e.g. Griffith et al., 1978; Stout et al., 1979; Richards and Arkin, 1981). These are based on the idea that deep convective clouds having higher tops (low temperatures) may produce more rain and on findings that the regions of rainfall tend to be correlated with bright (visible) and cold (infrared) clouds.

Kasahara et al. (1986) demonstrated that a stratification of radiative imagery data in terms of cloud types helps to establish useful relationships between infrared radiance and vertical motion. Nevertheless, the best correlation coefficient between IR temperature T_e and the lower tropospheric mean vertical \bar{p} -velocity $\bar{\omega}_a$ during the two 15-day periods for the northern hemisphere winter and summer in 1979 was 0.53. This value may be compared with the correlation coefficients (CC) obtained by other investigators when comparing infrared satellite data with observed rainfall rates. Although the range of values quoted in the literature varies widely, the maximum values are approximately 0.8 (e.g. Griffith et al.; Arkin, 1979). If we allow the hypothesis that satellite imagery data are as strongly correlated with vertical motions as are rainfall rates, then we

can interpret the difference in the CC values of 0.5 and 0.8 as an indication of inaccuracy in the vertical motion fields of the FGGE analyses for these periods. Note that vertical motions are quantities diagnosed from the analyses rather than ground truths measured directly by instruments. It is well known that the analysis of tropical wind fields is difficult due to the complicated relationship between the mass and velocity fields (Daley, 1985). Significant improvements are required in both the quality and quantity of the current meteorological observations in order to analyze accurately the irrotational part of the velocity in the tropics. At this point, it seems worthwhile to consider using satellite radiative imagery data to improve the analysis of the vertical motion field in the tropics. Julian (1984) proposed a scheme to estimate the divergent wind by transforming the satellite infrared radiation pattern into the velocity potential.

The purpose of this study is to propose a different procedure of estimating the divergent wind component in the tropics based on satellite radiometric imagery data.

2. Satellite radiometric data and synoptic background

In this study, as satellite radiometric imagery data, we use daytime and nighttime outgoing longwave radiation (OLR) data on 2.5° longitude-latitude grids processed from measurements taken by the NOAA polar orbiters (Gruber and Krueger, 1984). The use of these data as radiometric imagery data is made, not because these data are ideally suited for this study, but because they are readily available and provide a data set to formulate basic algorithms which can be improved later when more suitable radiometric data become available. In fact, the use of polar orbiter data is rather inconvenient for numerical weather prediction. Since the polar orbiters are sun-synchronous, the data for a given longitude represent a picture

at local standard time, which is dependent upon the equator crossing times of a particular spacecraft. In order to interpolate a data set for a standard map time of, say 1200 GMT, the daytime and nighttime measurements are linearly weighted according to the time of equator crossing. In this study, we adopted a procedure similar to one described in Julian (1984) to obtain interpolated 1200 GMT data from the daytime and nighttime flux data. The infrared data F , given in units of Wm^{-2} , are converted to equivalent blackbody temperature T_e using $F = \sigma T_e^4$, where $\sigma = 5.6693 \times 10^{-8} Wm^{-2} K^{-4}$.

Figure 1 shows the distribution of $258K - T_e$ for 1200 GMT, January 21, 1985. The constant value of 258K is chosen based on Kasahara et al. (1986), in which this constant value represents a threshold IR temperature separating the ascending and descending motion areas in the tropics. It will be assumed here that the positive (negative) areas delineated by solid (dashed) lines correspond to those of ascending (descending) motion. We see that the positive areas generally correspond to the intertropical convergence zone, which is shifted to the south of the equator during a boreal winter. The negative areas generally correspond to the subtropical highs, as seen in Fig. 2 which shows the stream function ψ at the sigma level $\sigma = 0.583$ for 1200 GMT January 21, 1985. The synoptic data used in this study were produced at the National Meteorological Center (c.f. Dey and Morone, 1985). Note that in Fig. 2 the subtropical high areas in the southern hemisphere are represented by minima in the stream function ψ field. In order to identify mid-latitude disturbances, the troughs (ridges) are denoted by solid (dashed) lines.

Figure 3 shows the analyzed vertical p -velocity $\omega (\equiv dp/dt)$ at the level $\sigma = 0.500$ for the same date, where p refers to the

pressure and t denotes time. We see an organized vertical motion pattern in the mid-latitudes, upward (downward) motion in front of the troughs (ridges) or behind the ridges (troughs). In the tropics, say between 25°N to 25°S , the pattern of vertical motion resembles somewhat the OLR pattern, but the ω -field over the South America, Atlantic and East Indies contains intense small scale irregularities.

Figure 4 shows the initialized ω , produced operationally at NMC by diabatic nonlinear normal mode initialization (B. Ballish, personal communication). We see that the ω -pattern in the mid-latitudes after initialization is enhanced compared with Fig. 3. However, the ω -pattern in the tropics after initialization becomes rather smooth and no longer appears similar to the satellite imagery pattern in Fig. 1. Since there is no reason to expect that the magnitude of vertical velocity in the tropics is so small compared with that of vertical motions in the mid-latitudes, the initialized ω -pattern in the tropics is clearly unrealistic. We therefore propose in the following an algorithm to modify the vertical motion field in a manner consistent with the satellite imagery data.

3. Determination of ω in descending motion areas.

We assume that the areas where $T_e > 258\text{K}$ are those of descending motion. The thermodynamic energy equation of the NMC operational global spectral model (Sela, 1980) can be written in the form

$$\frac{dT}{dt} - \sigma \frac{d \ln P_*}{dt} \frac{\partial T}{\partial \sigma} - \frac{\Gamma}{P_*} \omega = \frac{Q}{C_p}, \quad (3.1)$$

where T , P_* and ω denote, respectively, the temperature, surface pressure and vertical P -velocity ($\equiv dP/dt$). The vertical coordinate σ is defined by P/P_* . The individual derivative

with respect to time t is represented by $\frac{\partial}{\partial t} + \mathbf{V} \cdot \nabla$, where \mathbf{V} and ∇ denote, respectively, the horizontal velocity and horizontal gradient operator expressed in spherical coordinates in longitude λ and latitude ϕ . The term $\mathbf{V} \cdot \nabla$ represents horizontal advection. In (3.1), Γ denotes a static stability of the form

$$\Gamma = \frac{RT}{C_p \sigma} - \frac{\partial T}{\partial \sigma}, \quad (3.2)$$

where R and C_p represent, respectively, the gas constant and the specific heat of dry air at constant pressure. The right-hand side of (3.1) denotes the diabatic heating rate.

If we disregard diurnal variations, the time rates of change in T and P_* in the tropics are small. Fig. 5 shows the difference in the temperature T at $\sigma = 0.583$ between January 21-22, 1985, both at 1200 GMT. While in the mid-latitudes, temperature changes in one day are on the order of 10K, they are on the order of 1K in the tropics.

With the assumptions that $\frac{\partial T}{\partial t} = \frac{\partial P_*}{\partial t} = 0$ in (3.1), we obtain a diagnostic equation for ω in the form

$$\omega = \frac{P_*}{\Gamma} \left[-\frac{Q}{C_p} - \sigma (\mathbf{V} \cdot \nabla \ln P_*) \frac{\partial T}{\partial \sigma} + \mathbf{V} \cdot \nabla T \right] \quad (3.3)$$

This equation will be used to determine the value of ω in the descending motion areas.

Since the magnitude of the diabatic heating rate Q/C_p is also on the order of 1K, one may ask why Q/C_p is kept, but not $\frac{\partial T}{\partial t}$. The principle of data initialization is to adjust the initial conditions so that high-frequency oscillations do not develop during time integrations.

Since the value of ω is unknown in (3.1), while Q/C_p , $\mathbf{V} \cdot \nabla T$ and $\mathbf{V} \cdot \nabla \ln P_*$ are given by the analysis, we must ascertain that the determination of ω

will not cause large values of $\partial T / \partial t$. The simplest way to ensure that $\partial T / \partial t$ is bounded is to set $\partial T / \partial t$ to be zero. If one wishes to improve this constraint, it is possible to formulate a improved constraint by way of the bounded derivative approach (Kasahara, 1982).

The diabatic heating rate Q/C_p in the NMC global spectral model is calculated as the sum of various heating/cooling rates, involving the shortwave and longwave radiation, release of latent heat of condensation and sensible heat transfer from the earth surface. Radiative calculations utilize a zonal distribution of clouds (Campana, 1986). Since we are concerned with the determination of ω in cloud-free areas, we can ignore the effect of clouds in the radiation calculations for the present purpose. We also ignore the effect of shortwave absorption in the atmosphere, since we are not considering the effect of diurnal variations in the temperature field. The transfer of sensible heat from the earth surface can be a significant source of heating/cooling in the mid-latitudes. In the tropics, however, the sensible heat transfer effect is small in general, since air-sea temperature differences are usually small over the tropical oceans. Clearly, the longwave cooling term dominates in the diabatic heating rate Q/C_p in (3.3) in cloud-free regions in the tropics. Hence, for the evaluation of ω in descending motion areas, we will consider only the longwave cooling effect in Q/C_p .

4. Determination of ω in ascending motion areas

We assume that the areas where $T_e < 258$ K are those of moist convection and ascending motion, i.e. $\omega < 0$. We also assume the top of convection to be determined by the pressure level P_T corresponding to the value of T_e in tropical mean soundings. Between P_T and P_* , we assume that the profile of ω is given by

$$\omega(\sigma) = F(\sigma, P_T/P_*) , \quad (4.1)$$

where F represents a profile function of σ between $\sigma = 1$ and $\sigma_T = P_T/P_*$.

The determination of F in convective areas is divided into two steps. In the first step, we assume that the profile function F is represented by a parabola in the form

$$F = \omega_m z (z_T - z) / (z_T/2)^2 , \quad (4.2)$$

where

$$z = -\ln \sigma = -\ln (P/P_*) , \quad (4.3a)$$

$$z_T = -\ln \sigma_T = -\ln (P_T/P_*) , \quad (4.3b)$$

and ω_m denotes the minimum value (since ω is negative in the ascending region) at $Z = Z_T/2$.

The value of ω_m is determined by

$$\omega_m = \beta (T_{SH} - T) \quad (4.4)$$

where T_{SH} denotes the threshold temperature of 258K separating the ascending and descending regions. The coefficient β is chosen to be $-0.675 \times 10^{-4} \text{ hPa sec}^{-1} \text{ K}^{-1}$ after Kasahara et al. (1986).

In the second step, the profiles of ω in the ascending regions are further modified after imposing the conservation condition of total horizontal divergence, which will be discussed in the next section. Therefore, the final profiles of ω in the ascending regions after the second step will be slightly different from the form (4.2) assumed in the first step.

Above the top of convection, σ_T , the ω values are unchanged from those with which we started. In the synoptic example, which we will describe later, we use the initialized ω field as the starting point from which modifications are made in the tropical belt.

The ω -field is modified according to (3.3) and (4.1) at all levels except for the two lowest sigma levels and stratospheric levels. At the lowest sigma level ($\sigma=1$) and levels above $\sigma=0.140$, ω is left unmodified. At the second lowest sigma level, ω is left unchanged in descending regions; in ascending regions, the new ω is the average of the old ω and new ω as given by (4.1).

5. Determination of a new divergent wind field

Once the ω -field is modified, the horizontal divergence $D (= \nabla \cdot \mathbf{V})$ is calculated from

$$\frac{\omega}{P_*} = \sigma \mathbf{V} \cdot \nabla \ln P_* - \int_0^\sigma (D + \mathbf{W} \cdot \nabla \ln P_*) d\sigma. \quad (5.1)$$

It is an integral equation and a finite-difference algorithm is used to solve for D at discrete model levels. Only the rotational part of wind velocity is used to calculate $\mathbf{W} \cdot \nabla \ln P_*$.

We must ensure that the new divergence field is well blended with the old divergence field. At the first two rows inside the southern and northern boundaries of the tropical belt, the new D values are weighted by 1/3 and 2/3, respectively, to the old D values. This gives a smooth transition from the old D values outside of the tropical belt to the new D values inside.

A gradual vertical transition in the divergence field is made by weighting the new and old D values by factors of 2/3 and 1/3, respectively, at the lowest two levels adjacent to the ground.

The divergence field outside of the tropical belt remains unchanged

after modification. This means that the area integral of D at each level within the tropical belt should not change, since the global area integration of D must vanish. In order to ensure the conservation of total divergence within the tropical belt, the final D values are adjusted by a weight in proportion to the magnitude of D. Let D_0 and D_m denote the divergence before and after modification, respectively. Also, let

$$w_e = |D_m|, \quad (5.2)$$

then the final D values are calculated from

$$D = D_m - w_e D_{corr} \quad (5.3)$$

where

$$D_{corr} = \int_S (D_m - D_0) \cos \phi \, d\phi \, d\lambda / \int_S w_e \cos \phi \, d\phi \, d\lambda \quad (5.4)$$

and the integration domain S refers to the area of the tropical belt.

The velocity potential χ is calculated from

$$D = \nabla^2 \chi \quad (5.5)$$

and the eastward and northward wind components u and v are calculated from

$$\begin{aligned} u &= -\frac{1}{a} \frac{\partial \chi}{\partial \phi} + \frac{1}{a \cos \phi} \frac{\partial \chi}{\partial \lambda} \quad (\equiv U_R + U_D) \\ v &= \frac{1}{a \cos \phi} \frac{\partial \chi}{\partial \lambda} + \frac{1}{a} \frac{\partial \chi}{\partial \phi} \quad (\equiv V_R + V_D) \end{aligned} \quad (5.6)$$

The stream function ψ remains unchanged, so that the change in the wind velocity is due only to the new divergent component of wind.

The ω -field is then recalculated from (5.1) using the new wind field \mathbf{V} obtained from (5.6). Thus the final ω -field will be slightly different from the blended ω -field after combining the descending and ascending branches of ω as described in Sections 3 and 4.

6. Synoptic example

We shall continue to use the same synoptic case of 1200 GMT January 21, 1985 (as described in Section 2) in order to present the results of applying the modification process to the divergent wind field in the tropical belt between 23.7°N and S. We adopt the operationally initialized fields to be the analysis set upon which divergence modifications are made. One could choose the uninitialized fields to be the starting analysis. However, the initialized ω fields in the mid-latitudes are superior to the uninitialized fields. This is also the case for the divergence field. Fig. 6 shows the blended ω -field at $\sigma = 0.500$ after the modification process described in Sections 3, 4 and 5. This particular level of ω was chosen for presentation because the consequences of ω -field blending can be seen clearly in mid-tropospheric levels.

(a) Flow patterns at the level $\sigma = 0.250$

First, let us present the results of modification at the upper tropospheric level, $\sigma = 0.250$.

Fig. 7a shows the blended divergence field, which should be compared with Figs. 7b and 7c for the analyzed and initialized divergence fields, respectively, at the same level. No changes are made outside of the tropical belt, so we will confine the following discussions of comparison to the tropical belt. The blended divergence field resembles more closely the analyzed field than the initialized field. For example, strong divergence areas are seen in both Figs. 7a and b over South America, the central to western Pacific Ocean, South Africa and other regions; these exhibit good correspondence with the deep convective areas seen on the satellite imagery pattern (Fig. 1). However, the analyzed D field contains a great deal of small-scale irregularities. In

particular, rather intense irregularities are seen over New Guinea where a high mountain peak (1954 m) exists. It is likely that this mountain peak is causing these intense irregularities whether they are real or not. The small-scale irregularities are much reduced in the initialized D field. A clearer indication of the changes after modification is seen in Fig. 8a, which shows the blended divergent wind velocity field. This figure should be compared with Figs. 8b and c for the analyzed and initialized divergent wind fields, respectively, at the same level. The arrow shown on the right bottom of the figures denotes a vector length of 25m sec^{-1} . Fig. 8a shows more organized divergent motion over South America, Southwest Pacific Ocean, Indian Ocean, South Africa and other regions than Figs. 8b and c. However, the magnitude of the blended divergent wind over the Pacific (the western Indian Ocean) is smaller (larger) than that of the analyzed and initialized divergent wind over the same areas.

We will now examine the velocity potential χ field obtained from the relationship (5.5). Figs. 9a and b show the blended and analyzed χ fields, respectively. Major changes in the blended χ fields are (1) the reduction of positive values over the North Atlantic and the Northeast Pacific off the west coast of the U.S., and reduction of negative values over New Guinea, Phillipine and Borneo Islands, and (2) the intensification of positive values over the Indian Ocean and North Africa. These changes are expected from the incorporation of deep convection information seen in Fig. 1.

Figs. 10a and b show the differences between the blended and analyzed divergent wind components u_D and v_D , respectively. The contour intervals

are 2 m sec^{-1} . We see very small changes outside of the tropical belt, as expected. The differences in u_D range from -18 to 10 m sec^{-1} ; for v_D the range is from -18 to 20 m sec^{-1} . Except for a few locations over the oceans, the differences are generally smaller than 10 m sec^{-1} . Fig. 11a and b show the differences between the initialized and analyzed divergent wind components u_D and v_D , respectively. We see that the initialization alters the divergent velocity components in the range of $\pm 6 \text{ m sec}^{-1}$. Most of the initialization changes occur in the tropical belt.

Figures 12a and b show the total wind velocity components u and v after blending. The total wind velocity is the sum of the blended divergent wind velocity \mathcal{V}_D and the analyzed rotational velocity \mathcal{V}_R , of which the latter is unchanged by the modification.

Although the blending process yields larger changes in the divergent velocity field than does the initialization process, the fact that the initialization does not provide a satisfactory adjustment to the divergent velocity field implies that the impact of the blending process upon the analyzed divergent velocity field is expected to be larger than the impact of the initialization. Moreover, the magnitude of changes in the wind velocity is still very much smaller than the total wind velocity itself.

Although we should compare the blended total wind field with observations used in the objective analysis, the impact of the blending process upon the divergent wind field may be considered to be within analysis uncertainties.

(b) Flow patterns at the level $\sigma = 0.917$

We now present the results of modification at a lower tropospheric level, $\sigma = 0.917$, for the same case. This is the second lowest model level.

Fig. 13a shows the blended divergence field, which should be compared with Figs. 13b and c for the analyzed and initialized divergence fields, respectively. We see no changes outside of the tropical belt, as expected. The blended divergence field shows a much smoother pattern than the analyzed and initialized divergence fields. A closer examination, however, reveals that convergence areas are generally associated with the convective areas seen in Fig. 1.

We see more clearly the benefit of the blending process by examining the divergent velocity field. Fig. 14a shows the blended divergent wind velocity field, which should be compared with the analyzed and initialized divergent wind velocity fields in Figs. 14b and c. Neither the analyzed nor the initialized fields exhibit a clear indication of lower level convergence associated with the convective areas seen in Fig. 1.

We can also see the beneficial impact of the blending process at this level by comparing Figs. 15a and b, which show the blended and analyzed χ -fields, respectively. The superposition of Fig. 15a with Fig. 14a helps to identify the areas of convergence and divergence more easily than looking at the blended divergence field of Fig. 13a.

Figs. 16a and b show the differences between the blended and analyzed divergent velocity components u_D and v_D , respectively. The contour intervals are 2 m sec^{-1} . The differences in u_D range from -8 to 10 m sec^{-1} ; for v_D the range is from -6 to 8 m sec^{-1} . These differences are compared with the differences between the initialized and analyzed divergent velocity components u_D and v_D , shown on Figs. 17a and b, respectively. Note that the contour intervals used in Figs. 17a and b are 0.5 m sec^{-1} . The range of u_D differences is from -5.0

to 4.5 m sec^{-1} , and that of v_D differences is -4.5 to 5.5 m sec^{-1} . Although the impact of the blending process on the divergent wind at this level is slightly larger than that of the initialization, the modification required for the divergent wind velocity is within analysis uncertainties.

(c) Flow patterns at the level $\sigma = 0.583$

Since the ascending motions in deep convective areas in the tropics reach their maximum values in the mid-troposphere, and the descending motions in cloud-free areas are generally weak, it is reasonable to expect that the divergence is small in the tropical mid-troposphere.

Figs. 18a, b and c show, respectively, the blended, analyzed and initialized divergence fields at $\sigma = 0.583$. In contrast to the blended divergence field, both the analyzed and initialized fields contain small-scale irregularities with rather large magnitudes.

Fig. 19a shows the blended divergent wind velocity field, which should be compared with the analyzed divergent wind velocity field in Fig. 19b. The analyzed divergent wind field in the tropics is clearly unreasonable, having a rather intense disorganized pattern. The initialized divergent wind field, which is not shown, exhibits about the same appearance as the analyzed divergent wind field in the tropics. The blending process eliminated these intense tropical irregularities. Elimination of the noise in the mid-tropospheric divergence field should allow deep cumulus convection to occur when the lower and upper level divergent flow conditions are favorable.

7. Discussion

The procedure for modifying divergent motion in the tropics described

here produces a new tropical divergent wind field which appears to be an improvement over the initialized divergent wind field. At present, the degree of improvement rests upon a synoptic judgement that the modified divergent wind field should be consistent with the deep tropical convection seen from satellite imagery cloud patterns. Clearly, we need a more quantitative appraisal of improvement to judge the effectiveness of the proposed scheme. Since the final product is the total wind field, we can ask how well the blended wind field will fit the observations. Of course, we must use all wind observations, including those rejected during the data assimilation cycle, since it may be possible that data are rejected due to their poor fit to first guess values rather than their being inaccurate observations.

Ultimately, the quality of the blended wind field must be judged by making a forecast. Since we have modified the divergent wind field after the operational initialization, we must reinitialize the flow before a model run. One way to keep the blended divergence field along with the rotational wind field and temperature field (ignoring the question of the moisture field for a moment) is to apply the nonlinear normal mode initialization scheme in reverse so that the diabatic heating term in the initialization is determined as a residual. If such a diagnostically determined diabatic heating pattern were identical to the diabatic heating rate produced by the prediction model initially, then the blended divergence field would smoothly evolve with time during a model run. However, this situation will not happen unless the problem of physical initialization discussed in the Introduction can be solved. Meanwhile, we must resort to a temporal expedient to force the model to accept the specified initial conditions.

In Kasahara et al. (1986), we described a diagnostic method to evaluate diabatic heating rates as a residue of the thermodynamic equation using a time sequence of global analyses. Here, we will apply a similar technique to evaluate the initial diabatic heating term Q/C_p based on (3.1). The local time rate of change in temperature ($\partial T / \partial t$) will be estimated from the forward time tendency $\Delta T / \Delta t$ using two analyzed temperature fields of Δt apart. With reference to Fig. 5, our first experiment will be made using $\Delta t = 24$ hours. A similar method will be used to estimate $\partial \ln R_x / \partial t$. Once these initial tendencies are obtained from the forward time differences, the rest of the terms on the left-hand side of (3.1) will be calculated using the initial conditions. Hence, the initial heating term Q/C_p can be obtained.

The diagnosed heating rate Q/C_p will be specified during the time integration for a period of say, 6 hours, replacing the model generated diabatic heating term in the thermodynamic equation. Beyond the initial forcing period, the model generated heating rate will be used. This type of nudging has been applied successfully in forecast experiments. In order to augment diabatic heating rates during the spin-up period, Danard (1985) replaced the model generated condensation heating during the first six hours of the forecast period by an estimated heating from satellite infrared imagery data. T. Kudo, M. Ueno and T. Taira (of the Japan Meteorological Agency) also reported the beneficial effect of condensation heat nudging (Personal communication, 1986). They forced the prediction model for the first hour by using diagnosed condensation heating rates estimated from a combination of observed precipitation and satellite radiative imagery data.

We assumed in this study that the 2.5° resolution NOAA polar orbiter OLR data can provide (1) the division between convective (upward motion) and clear sky (downward motion) areas and (2) the height of convection cells. While the second assumption is less objectionable, the first assumption may be more problematic. As seen from Fig. 1, the 258K contours delineate the regions of upward and downward motions. Since the contour intervals are 5K in temperature, the use of a threshold temperature which differs from 258K by a few degrees may not change the overall pattern of the blended divergence field due to the conservation constraint on the total divergence in the tropical belt. The problem, however, is that the 2.5° resolution data may be more appropriate to resolve a planetary-scale vertical motion field than it is to represent small tropical disturbances. Although it is questionable whether or not the operationally analyzed divergence field can realistically describe the vertical motion fields associated with cloud clusters in the tropics, the resolution of satellite OLR data should be fine enough to identify the spatial scale of cloud clusters.

Related to the question of horizontal resolution of OLR data is a question concerning the time resolution of OLR data. We used in this test example OLR data interpolated from daytime and nighttime measurements to coincide with a synoptic map time. Although this procedure may be adequate for the 2.5° resolution data, multiple polar-orbiting satellite measurements with a more refined time-interpolation scheme are needed to identify the vertical motion field on the scale of cloud clusters. We will explore the use of the Geostationary Operational Environmental Satellite-WEST (GOES-W) data archived at the Colorado State University for the same test date. Although the GOES data cover only a portion of the globe, the

improved resolution in both space and time are needed to investigate the importance of small-scale vertical motion for numerical weather prediction in the tropics.

8. Conclusions

The divergent (irrotational) part of wind velocity is crucial for describing major features of the tropical circulation. However, accurate analysis of the divergent wind field is difficult in the tropics due to the complicated relationship between the mass and velocity fields. The current operational initialization procedure adds an additional difficulty; it significantly reduces the intensity of vertical circulations in the tropics.

In this report, we proposed a scheme to infer the divergent wind field in the tropics based on the 2.5° resolution NOAA polar orbiter OLR data. The scheme is regarded as a modification to the initialized divergent wind field in the tropics. Briefly speaking, the modification procedure is as follows: The intensity of ascending motion in deep convective areas is determined from a relationship between vertical motion and infrared equivalent blackbody temperature. The intensity of descending motion is estimated from the thermodynamic balance between radiative cooling and adiabatic warming, since the local time change of temperature is small in the tropics. Once the vertical motion field is determined, the horizontal divergence field can be calculated from the mass continuity equation; thus, the divergent part of wind is obtained.

This scheme was applied to the NMC analysis data set of January 21, 1985. The magnitude of change in the divergent wind field is on the order of analysis uncertainty. Hence, the modified divergent wind field is an

improvement over the existing analysis, since additional OLR information is incorporated in the final product.

The scheme described here can be looked upon as a means of quality control for analysis of the divergent wind field. Also, the proposed scheme can be incorporated into the current objective analysis-initialization procedure. Future directions of research to improve upon the proposed scheme are discussed in Section 7.

Acknowledgments

This work was conducted at the National Meteorological Center, Washington, D.C. during A. Kasahara's collaborative leave from the National Center for Atmospheric Research (NCAR) under the University Corporation for Atmospheric Research (UCAR) Visiting Scientist Program. Partial support for this research has been provided through the National Oceanic and Atmospheric Administration under No. NA85AAG02575. The authors are grateful to the staff members of the Development Division, NMC for technical assistance in carrying out this research.

REFERENCES

- Arkin, P.A., 1979: The relationship between fractional coverage of high cloud and rainfall accumulations during GATE over the B-scale array. Mon. Wea. Rev. , 107, 1382-1387.
- Campana, K. A., 1986: An approximation to the diurnal cycle for use in NMC's Medium-Range Forecast Model. Medium-Range Modeling Branch Note.
- Daley, R., 1985: The analysis of synoptic scale divergence by a statistical interpolation scheme. Mon. Wea. Rev., 113, 1066-1079.
- Dey, C. H., and L. L. Morone, 1985: Evolution of the National Meteorological Center global data assimilation system: January 1982 - December 1983. Mon. Wea. Rev., 113, 304-318.
- Donner, L., 1986: An initialization for cumulus convection in numerical weather prediction. Unpublished Notes.
- Errico, R.M., 1984: The dynamical balance of a general circulation model. Mon. Wea. Rev., 112, 2439-2454.
- _____, and P. J. Rasch, 1985: A comparison of various normal mode initialization schemes and the inclusion of diabatic processes. NCAR MS NO. 0501/85-7.
- Flattery, T., 1971: Spectral models for global analysis and forecasting. Proc. Sixth AWS Technical Exchange Conference, U.S. Naval Academy, Annapolis, MD. 21-24 September 1970, Air Weather Service Tech. Rep. 242, 42-54.
- Girard, C., and M. Jarraud, 1982: Short and medium range forecast differences between a spectral and grid point model. An extensive

- quasi-operational comparison. Technical Report No. 32, European Centre for Medium Range Weather Forecasts. 176 pp.
- Griffith, C. G., W. L. Woodley, P. G. Grube, D. W. Martin, J. Stout, and D. Sikdar, 1978: Rain estimation from geosynchronous satellite imagery-visible and infrared studies. Mon. Wea. Rev., 106, 1153-1171.
- Gruber, A., and A. F. Krueger, 1984: The status of the NOAA outgoing longwave radiation data set. Bull. Amer. Met. Soc., 65, 958-962.
- Heckley, W. A., 1985: The performance and systematic errors of the ECMWF tropical forecasts (1982-1984). Technical Report No. 53, European Centre for Medium Range Weather Forecasts, 97 pp.
- Julian, P.A., 1984: Objective analysis in the tropics: A proposed scheme. Mon. Wea. Rev., 112, 1752-1767.
- _____, 1985: Some comparisons of ECMWF IIIb and GFDL III b analyses in the tropics. Proc. First National Workshop on the Global Weather Experiment. Vol. I, National Academy Press, 211-216.
- Kasahara, A., 1982: Nonlinear normal mode initialization and the bounded derivative method. Rev. Geophys. Space Phys., 20, 385-397.
- _____, A. P. Mizzi and U. C. Mohanty, 1986: Comparison of global diabatic heating rates from FGGE LEVEL III b analyses with satellite radiation imagery data. Submitted to Mon. Wea. Rev.
- Krishnamurti, T. N., and Y. Ramanathan, 1982: Sensitivity of the monsoon onset to differential heating. J. Atmos. Sci., 39, 1290-1306.
- _____, S. Cooke, R. Pasch, and S. Low Nam, 1983: Precipitation estimates for rain gauge and satellite observations. Florida State University, Tallahassee, Florida, 32306, 373 pp.
- _____, K. Ingles, S. Cooke, T. Kitade, and R. Pasch, 1984: Details of low

latitude medium range numerical weather prediction using a global spectral model: Part II, Effects of orography and physical initialization.

J. Meteor. Soc. Japan, Ser. II, 62, 613-649.

Lorenc, A. C. 1984: The evolution of planetary-scale 200 mb divergence flow during the FGGE year. Quart. J. R. Met. Soc., 110, 427-441.

McPherson, R. D., K. H. Bergman, R. E. Kistler, G. E. Pasch and D. S. Gordon, 1979: The NMC operational global data assimilation system. Mon. Wea. Rev., 107, 1445-1461.

Mohanty, U. C., A. Kasahara, and R. Errico, 1986: The impact of diabatic heating on the initialization of a global forecast model. To appear in J. Meteor. Soc. Japan, Ser. II.

Murakami, T., and Y. H. Ding, 1982: Wind and temperature changes over Eurasia during the early summer of 1979. J. Meteor. Soc. Japan, 60, 183-196.

Paegle, J., and W. E. Baker, 1982: Planetary-scale characteristics of the atmospheric circulation during January and February 1979. J. Atmos. Sci., 39, 2521-2538.

Richards, F., and P. Arkin, 1981: On the relationship between satellite-observed cloud cover and precipitation. Mon. Wea. Rev., 109, 1081-1093.

Sela, J. G. 1980: Spectral modeling at the National Meteorological Center. Mon. Wea. Rev., 108, 1279-1292.

Stout, J. E., D. W. Martin, and D. N. Sikdar, 1979: Estimating GATE rainfall with geosynchronous satellite images. Mon. Wea. Rev., 107, 585-598.

Wergen, E., 1983: Initialization. Interpretation of numerical weather prediction product. ECMWF Seminar/Workshop 1982, 31-57.

LEGENDS

- Fig. 1. Pattern of $258K - T_e$, where T_e is IR temperature in K for 1200 GMT, January 21, 1985. Contour interval is 5K. Positive (negative) areas delineated by solid (dashed) lines are those colder (warmer) than 258K.
- Fig. 2. Stream function Ψ at the sigma level $\sigma = 0.583$ for 1200 GMT, January 21, 1985.
- Fig. 3. Analyzed vertical p -velocity (hPa sec^{-1}) at the level $\sigma = 0.500$ for the same date as in Fig.2.
- Fig. 4. Initialized vertical p -velocity (hPa sec^{-1}) at the same level and date as in Fig. 3.
- Fig. 5. One day temperature difference (K) at $\sigma = 0.583$ between January 22-21, 1985 both at 1200 GMT.
- Fig. 6. Blended ω -field (hPa sec^{-1}) at $\sigma = 0.500$ for 1200 GMT, January 21, 1985. Compare this figure with Figs. 3 and 4.
- Fig. 7. (a) Blended divergence field (sec^{-1}) at $\sigma = 0.250$ for 1200 GMT January 21, 1985. (b) Analyzed divergence field (sec^{-1}) at the same level and date as (a). (c) Initialized divergence field (sec^{-1}) corresponding to (b).
- Fig. 8. (a) Blended divergent wind velocity field (m sec^{-1}) at $\sigma = 0.250$ for 1200 GMT January 21, 1985. (b) Analyzed divergent velocity field at the same level and date as (a). (c) Initialized divergent velocity field corresponding to (b).
- Fig. 9. (a) Blended velocity potential field derived from the blended divergence field shown in Fig. 7a. (b) Analyzed velocity potential field derived from the analyzed divergence field shown in Fig. 7b.

- Fig. 10. (a) Difference field (m sec^{-1}) between the blended and analyzed east-west divergent velocity components at $\sigma = 0.250$. (b) Same as (a), but for the north-south velocity component.
- Fig. 11. (a) Difference field (m sec^{-1}) between the initialized and analyzed east-west divergent velocity components at $\sigma = 0.250$. (b) Same as (a), but for the north-south velocity component.
- Fig. 12. (a) Total wind u velocity component (m sec^{-1}) after the divergence blending at $\sigma = 0.250$. (b) Same as (a), but for the v velocity component (m sec^{-1}).
- Fig. 13. (a) Blended divergence field (m sec^{-1}) at $\sigma = 0.917$. (b) Analyzed divergence field at the same level as (a). (c) Initialized divergence field corresponding to (b).
- Fig. 14. (a) Blended divergent wind velocity field (m sec^{-1}) at $\sigma = 0.917$. (b) Analyzed divergent velocity field at the same level as (a). (c) Initialized divergent velocity field corresponding to (b).
- Fig. 15. (a) Blended velocity potential field derived from the blended divergence field shown in Fig. 13a. (b) Analyzed velocity potential field derived from the analyzed divergence field shown in Fig. 13b.
- Fig. 16. (a) Difference fields (m sec^{-1}) between the blended and analyzed east-west divergent velocity components at $\sigma = 0.917$. (b) Same as (a), but for the north-south component.
- Fig. 17. (a) Difference field (m sec^{-1}) between the initialized and analyzed east-west divergent velocity components at $\sigma = 0.917$. (b) Same as (a), but for the north-south velocity component.

Fig. 18. (a) Blended divergence field (sec^{-1}) at $\sigma = 0.583$. (b) Analyzed divergence field at the same level as (a). (c) Initialized divergence field corresponding to (b).

Fig. 19. (a) Blended divergent wind velocity field (m sec^{-1}) at $\sigma = 0.583$. (b) Analyzed divergent velocity field corresponding to (a).

UVKH(12Z,AFTVI) LEVEL 8 1/21/85 SIG=0.583

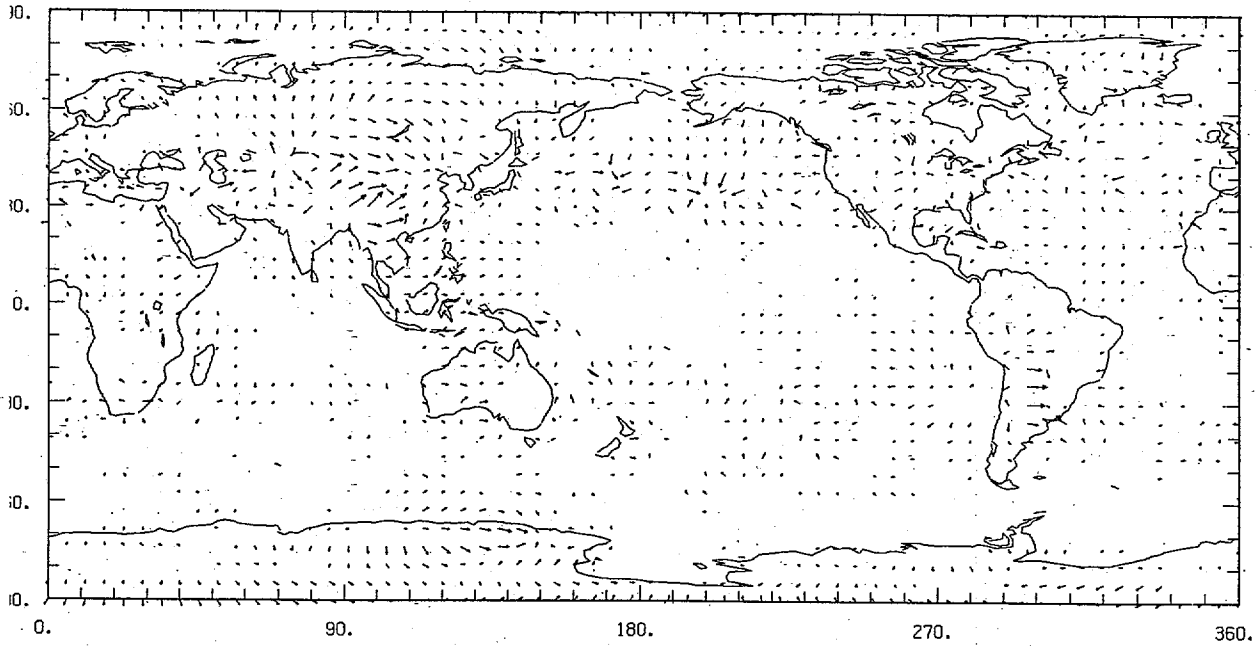


Fig. 19 a Blended divergent wind velocity at $\sigma = 0.583$

0.250E+02
MAXIMUM VECTOR
m sec⁻¹

UVKH(12Z,ANA.) LEVEL 8 1/21/85 SIG=0.583

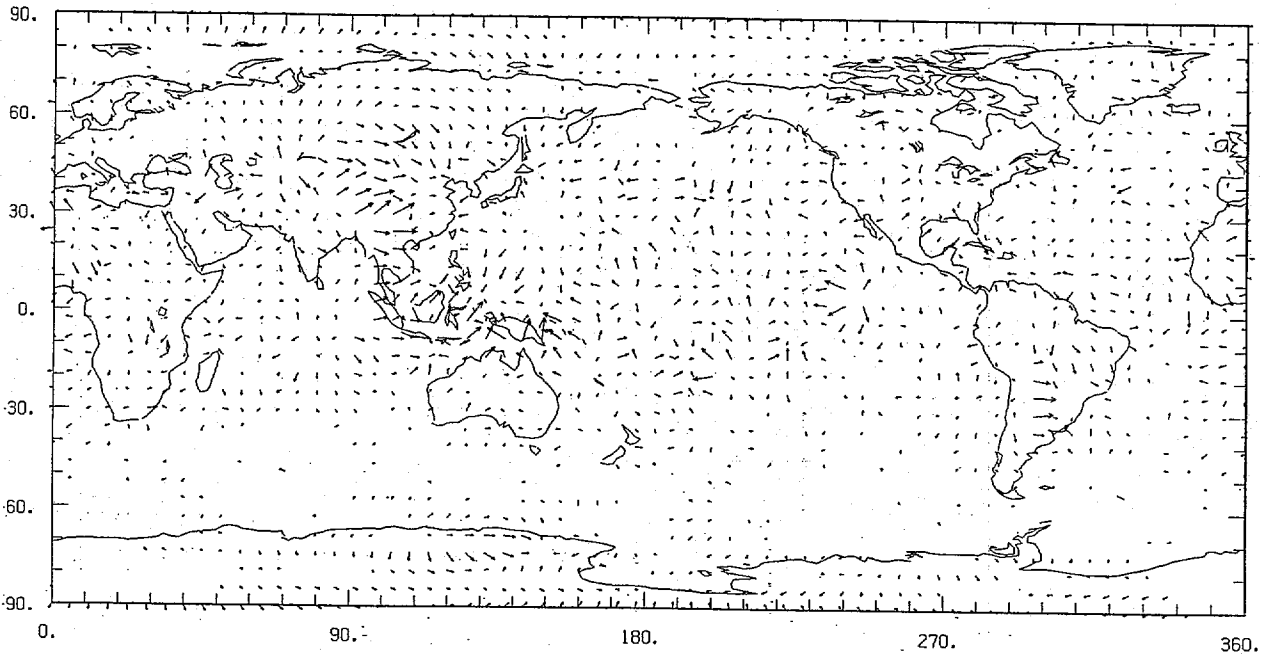
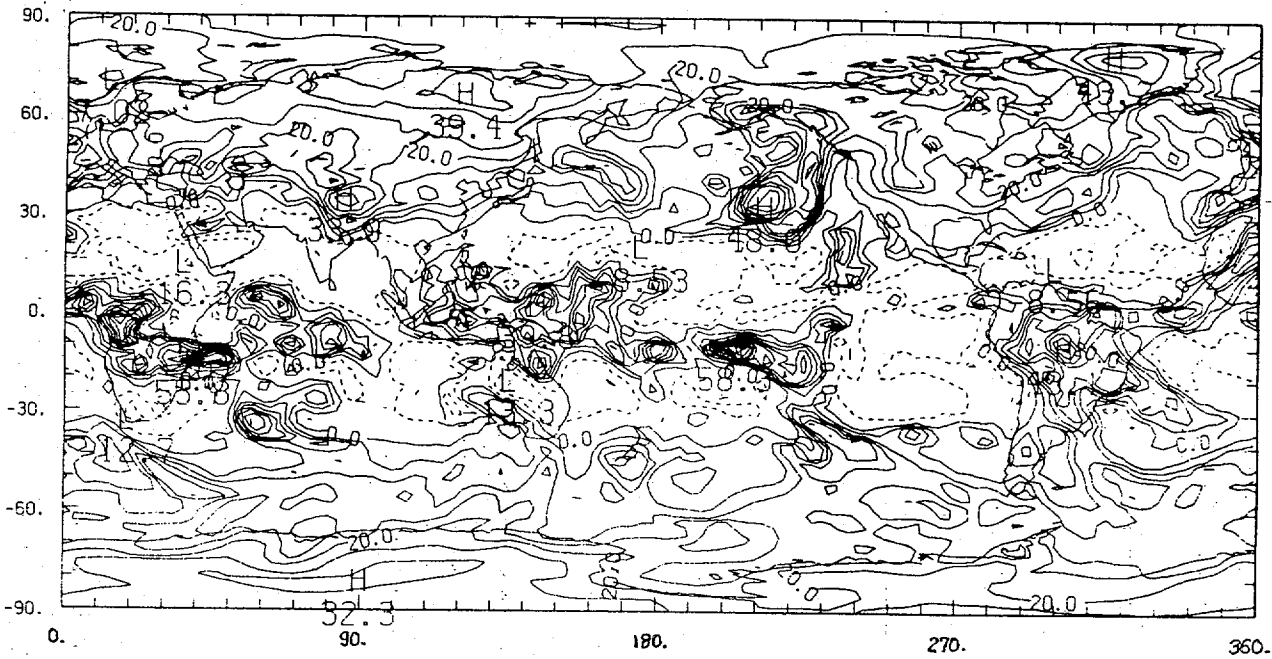


Fig. 19 b Analyzed divergent wind velocity at $\sigma = 0.583$

0.250E+02
MAXIMUM VECTOR
m sec⁻¹

T0LR

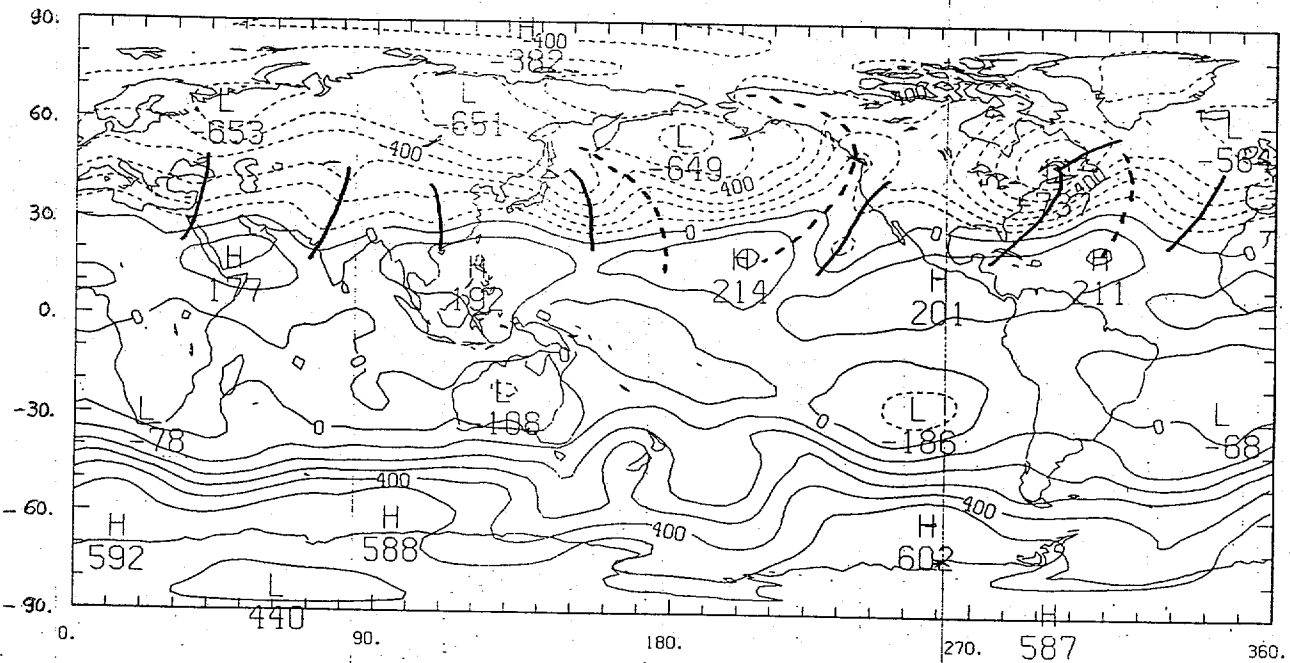
12Z 1/21/85



CONTOUR FROM -15.000 TO 55.000 CONTOUR INTERVAL OF 5.0000 PT(3,3)= 25.520

Fig. 1 258 K - Te 12GMT Jan. 21, 85

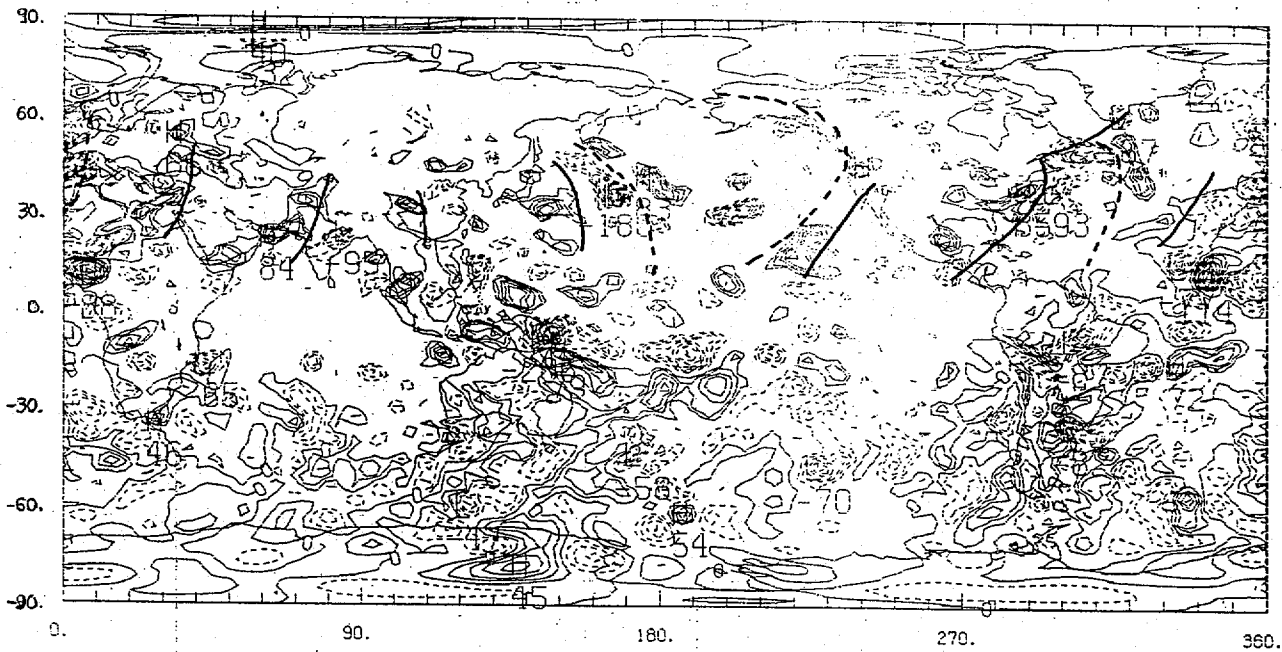
SI(12Z, IN) AT LEVEL 8 1/21/85 SIG=0.583



CONTOUR FROM -0.70000E+08 TO 0.60000E+08 CONTOUR INTERVAL OF 0.10000E+08 PT(3,3)= 0.53512E+08 LABELS SCALED BY 0.10000E-04

Fig. 2 Stream function ψ at $\sigma = 0.583$ 12GMT 1/21/85

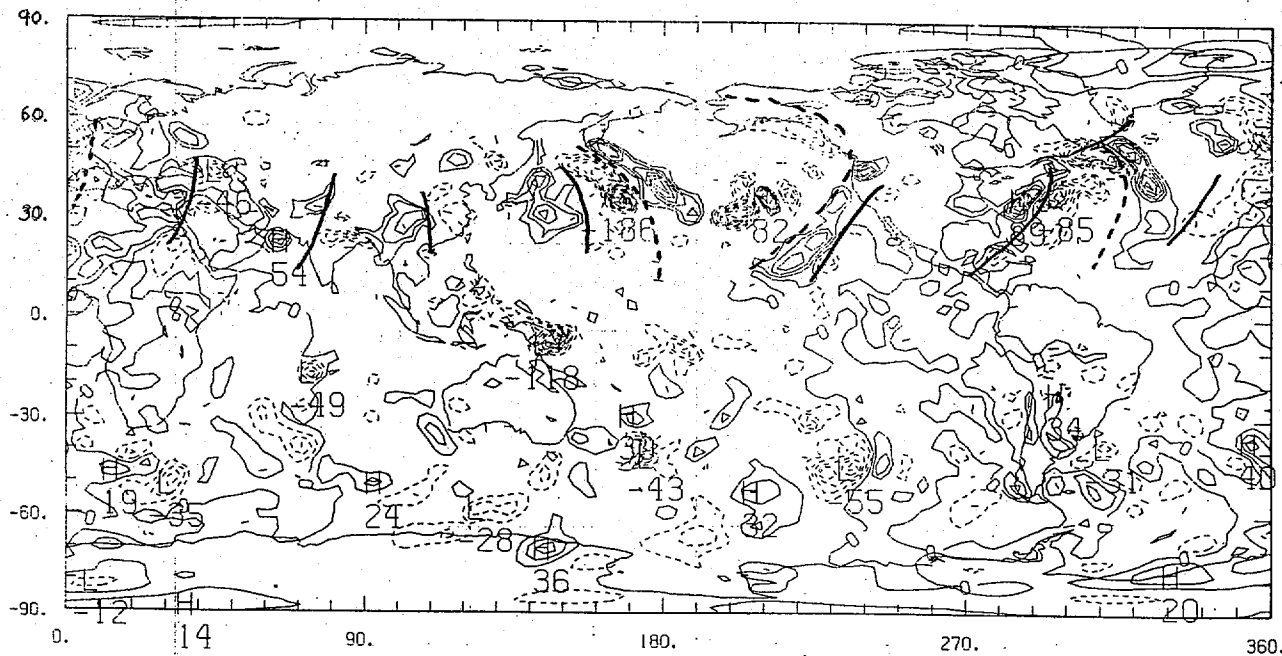
OMEGA - 12Z AT LEVEL 10 1/21/85 SIG=0.500



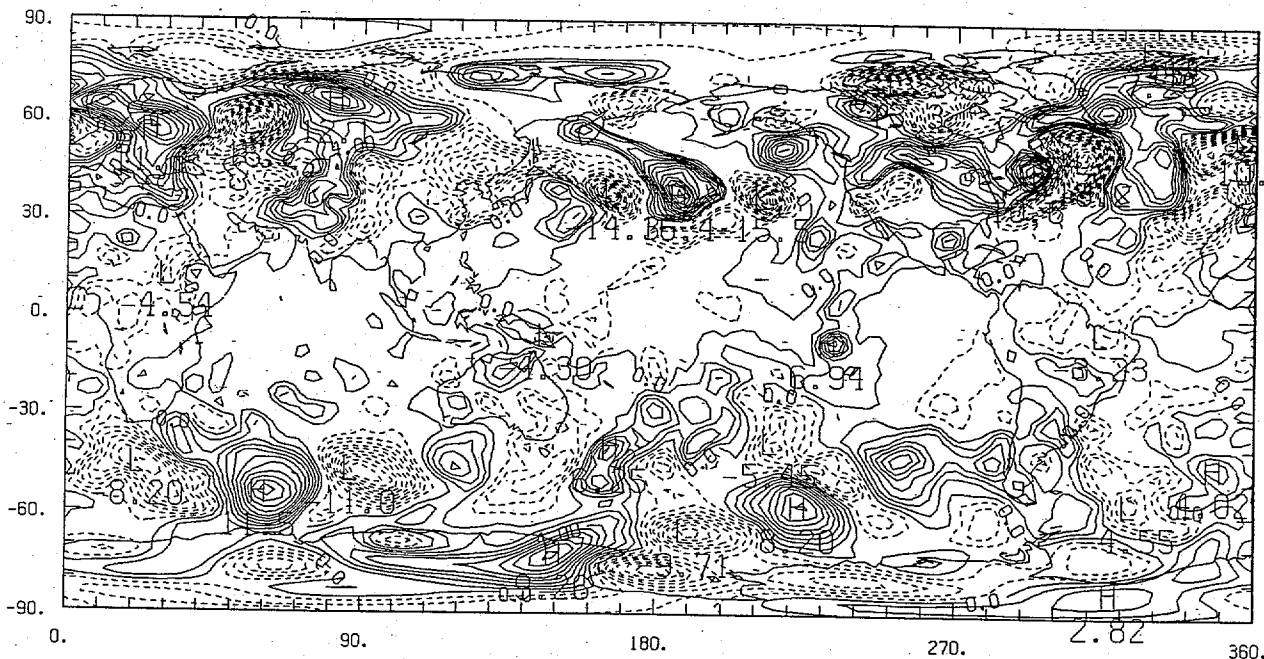
CONTOUR FROM -0.20000E-01 TO 0.11000E-01 CONTOUR INTERVAL OF 0.10000E-02 PT(3,3)= 0.54988E-03 LABELS SCALED BY 10000.

Fig. 3 Analyzed ω ($\equiv dp/dt$) at $\sigma = 0.500$ 12GMT 1/21/85

OMEGA(I) 12Z AT LEVEL 10 1/21/85 SIG=0.500



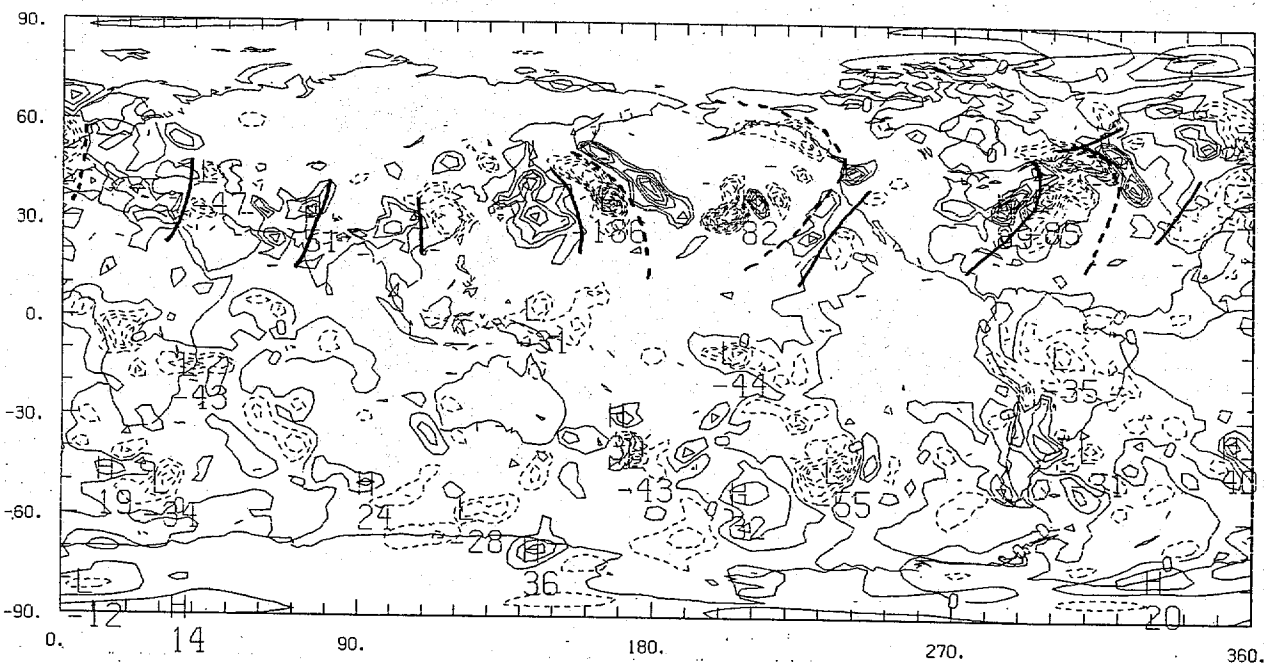
DTEM(12Z)/DT AT LEVEL 8 1/21/85 SIG=0.583



COUNTUR FROM -18.000 TO 16.000 COUNTUR INTERVAL OF 1.0000 PT(3,3)= -1.5400

Fig. 5 One day temperature difference between Jan. 22-21, 85 at $\sigma = 0.583$

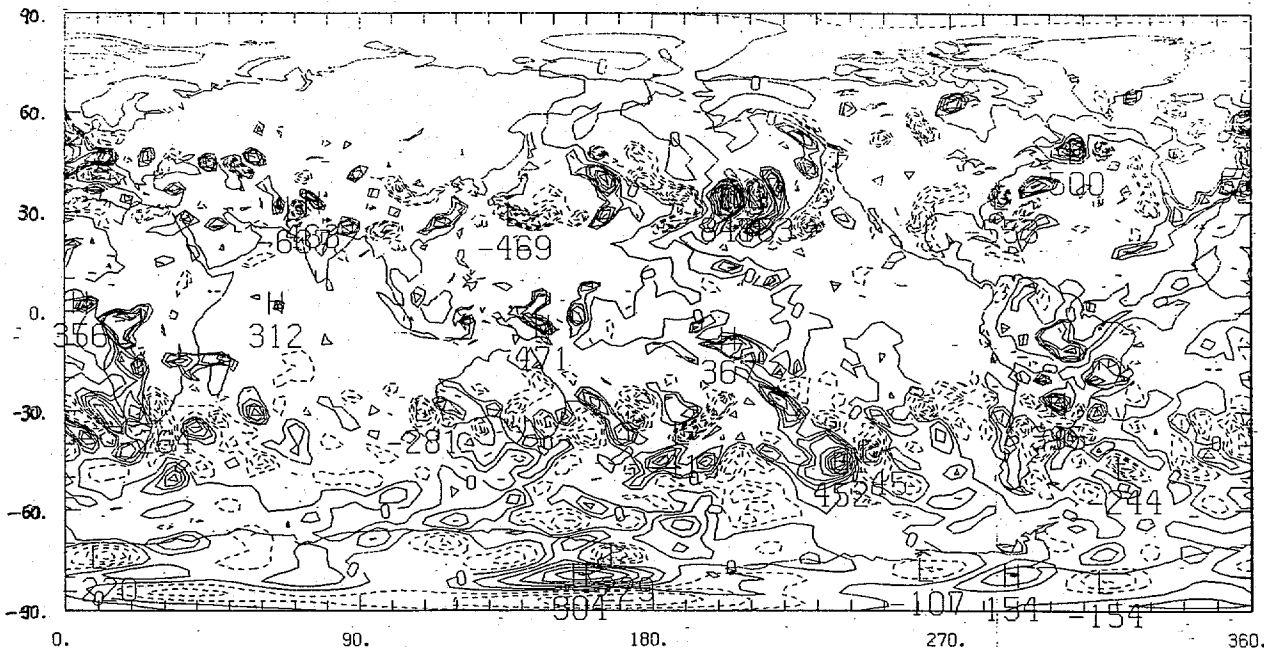
OMGA(12Z.NE) AT LEVEL 10 1/21/85 SIG=0.500



COUNTUR FROM -0.18000E-01 TO 0.80000E-02 COUNTUR INTERVAL OF 0.10000E-02 PT(3,3)= 0.67919E-03 LABELS SCALED BY 10000.

Fig. 6 Blended ω at $\sigma = 0.500$ 12GMT 1/21/85

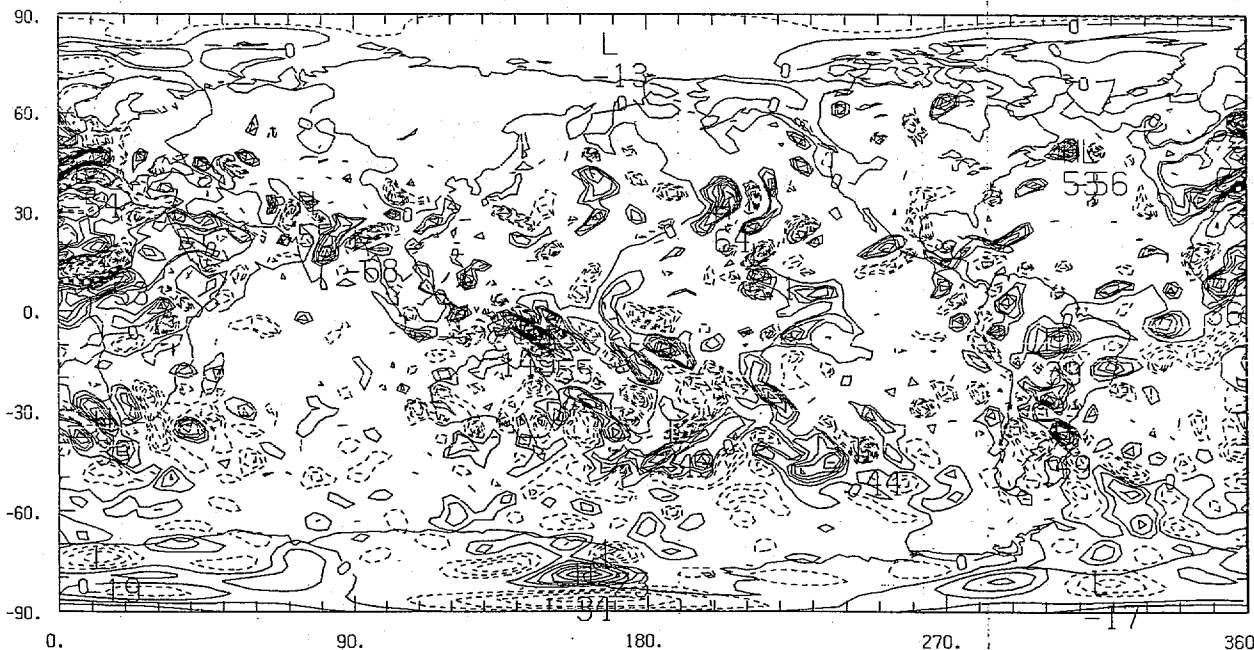
DIV(12Z.AFTVI) LEVEL 14 1/21/85 SIG=0.250



CONTOUR FROM -0.85000E-04 TO 0.80000E-04 CONTOUR INTERVAL OF 0.50000E-05 PT(3,3)= 0.42023E-05 LABELS SCALED BY 0.10000E+08

Fig. 7a Blended divergence D at $\sigma = 0.250$ 12GMT 1/21/85

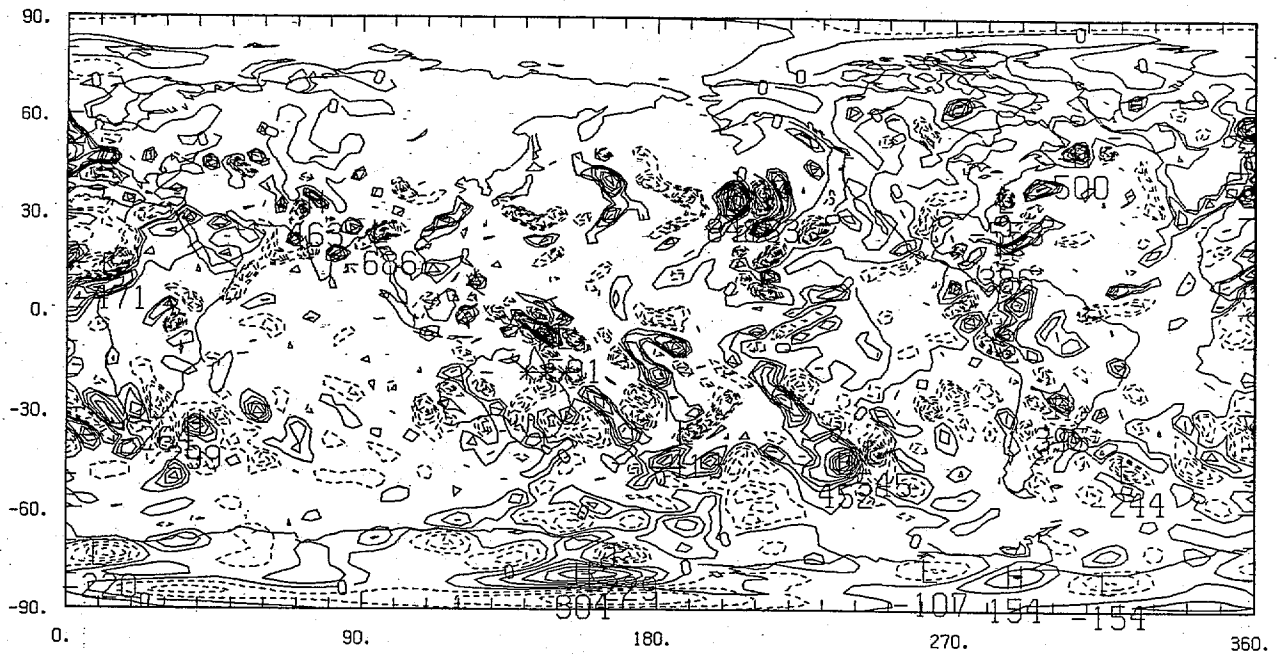
DIV(12Z.ANA.) LEVEL 14 1/21/85 SIG=0.250



CONTOUR FROM -0.70000E-04 TO 0.12500E-03 CONTOUR INTERVAL OF 0.50000E-05 PT(3,3)= 0.34093E-05 LABELS SCALED BY 0.10000E+07

Fig. 7b Analyzed divergence at $\sigma = 0.250$ 12GMT 1/21/85

DIVE(12Z,IN) AT LEVEL 14 1/21/85 SIG=0.250



COUNTOUR FROM -0.85000E-04 TO 0.10000E-03 COUNTOUR INTERVAL OF 0.50000E-05 PT(3,3)= 0.42023E-05 LABELS SCALED BY 0.10000E+08

Fig. 7 C Initialized divergence at $\sigma = 0.250$ 12GMT 1/21/85

UVKH(12Z,AFTVI) LEVEL 14 1/21/85 SIG=0.250

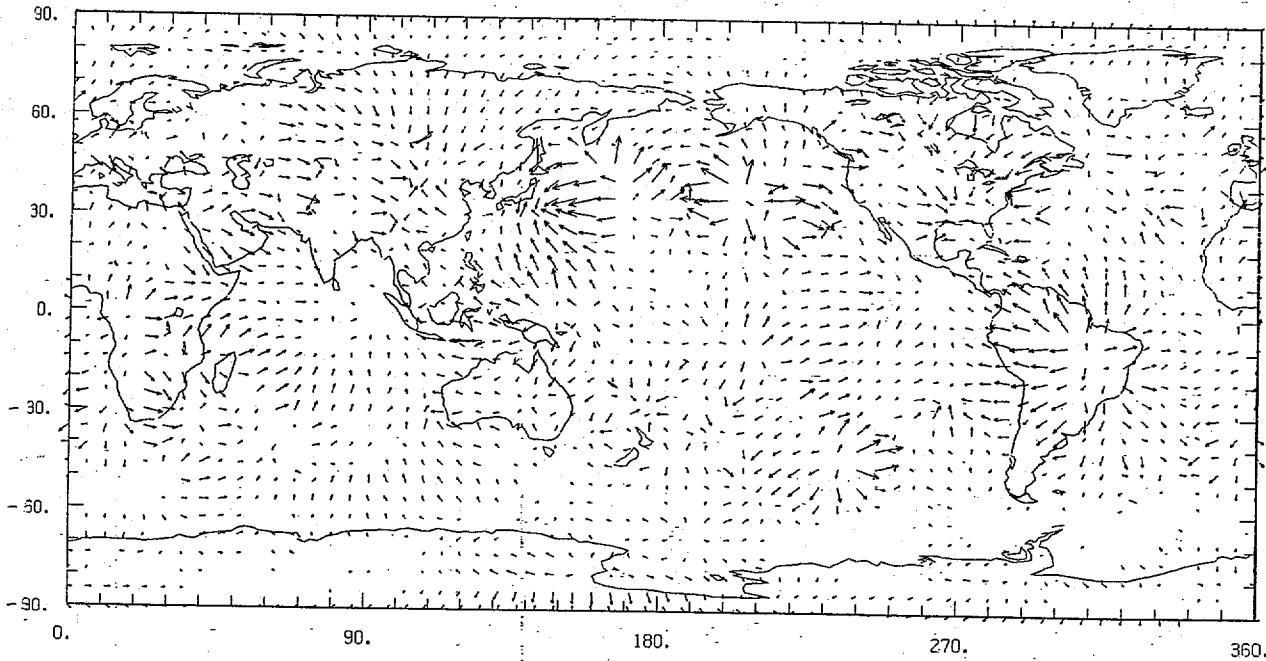


Fig. 8 a Blended divergent velocity $m sec^{-1}$
at $\sigma = 0.250$ 12 GMT 1/21/85

0.250E+02
MAXIMUM VECTOR

UVKH(12Z,ANA.) LEVEL 14 1/21/85 SIG=0.250

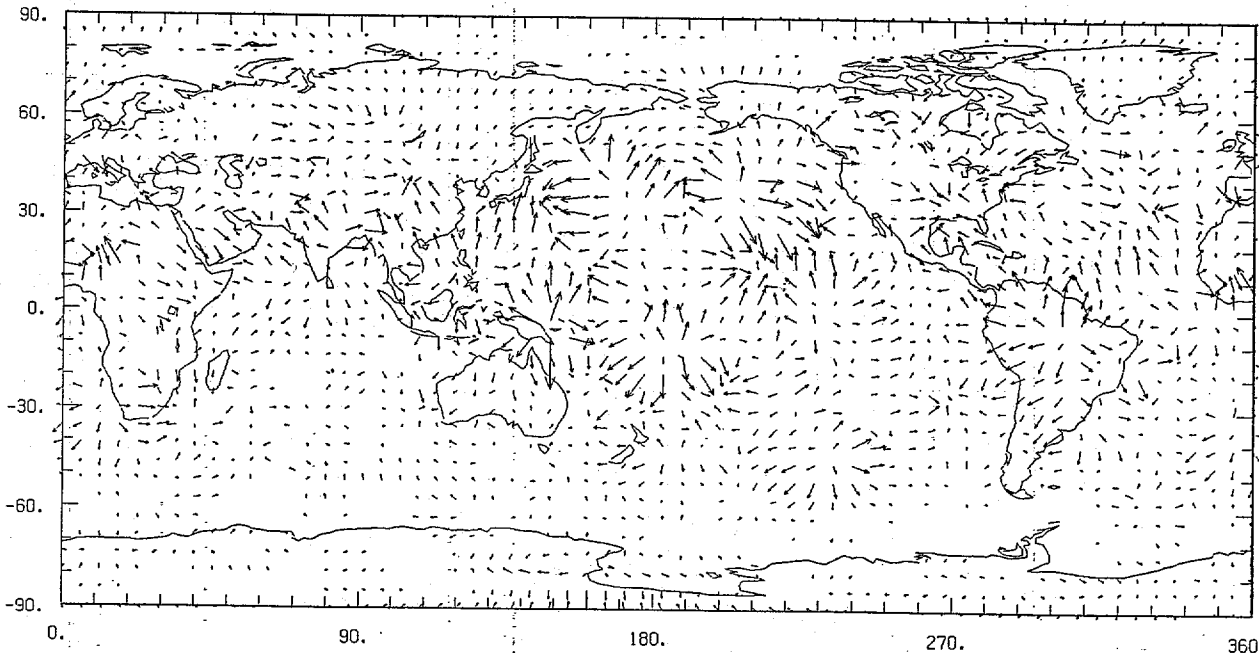


Fig. 8 b Analyzed divergent velocity $m sec^{-1}$
at $\sigma = 0.250$ 12 GMT 1/21/85

0.250E+02
MAXIMUM VECTOR

UVKH(12Z,INI.) LEVEL 14 1/21/85 SIG=0.250

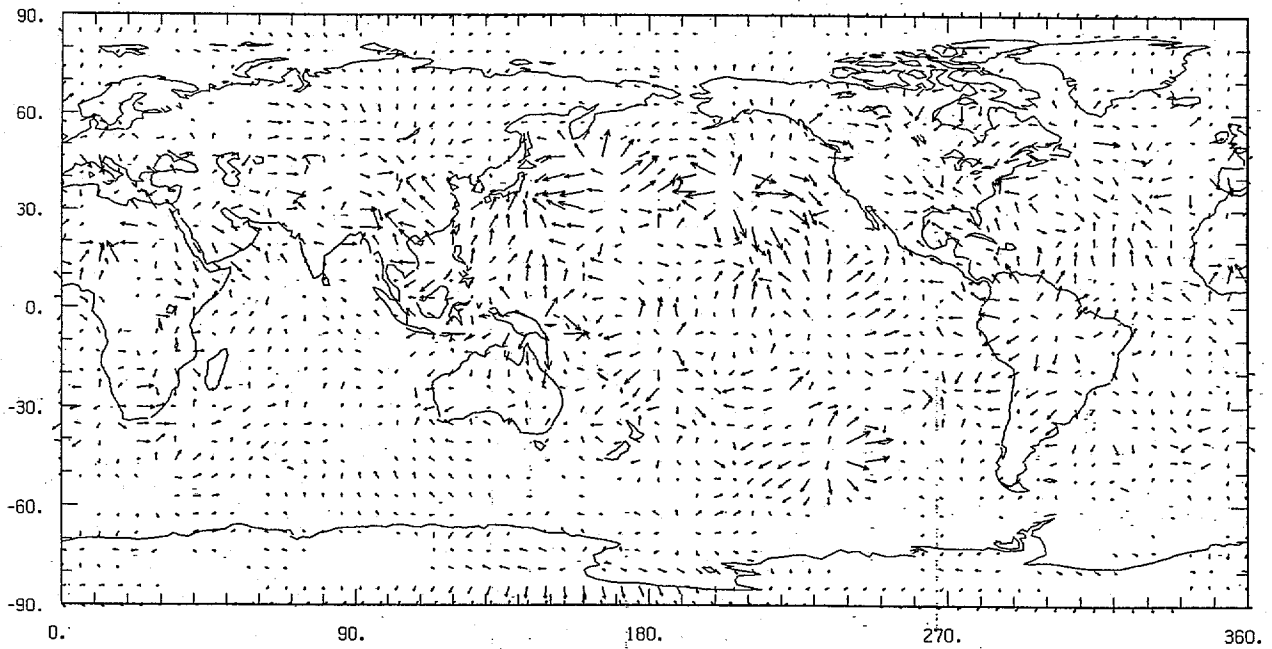
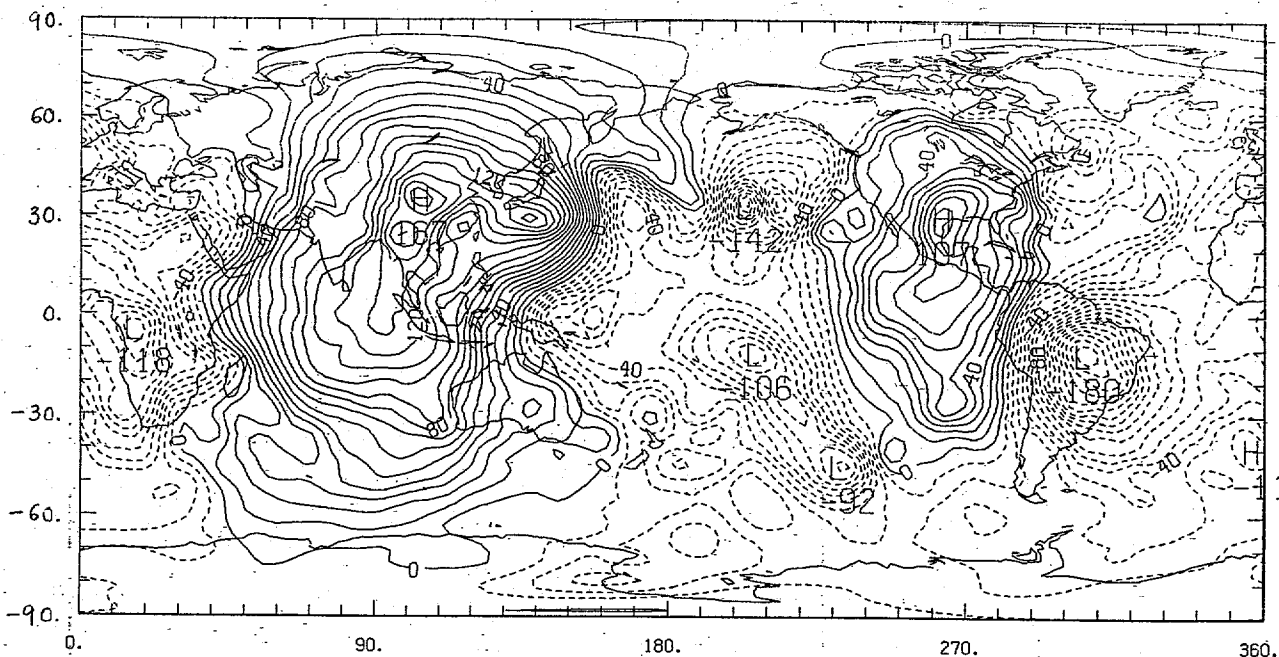


Fig. 8c Initialized divergent velocity $m\ sec^{-1}$
at $\sigma = 0.250$ 12 GMT 1/21/85

0.250E+02
MAXIMUM VECTOR

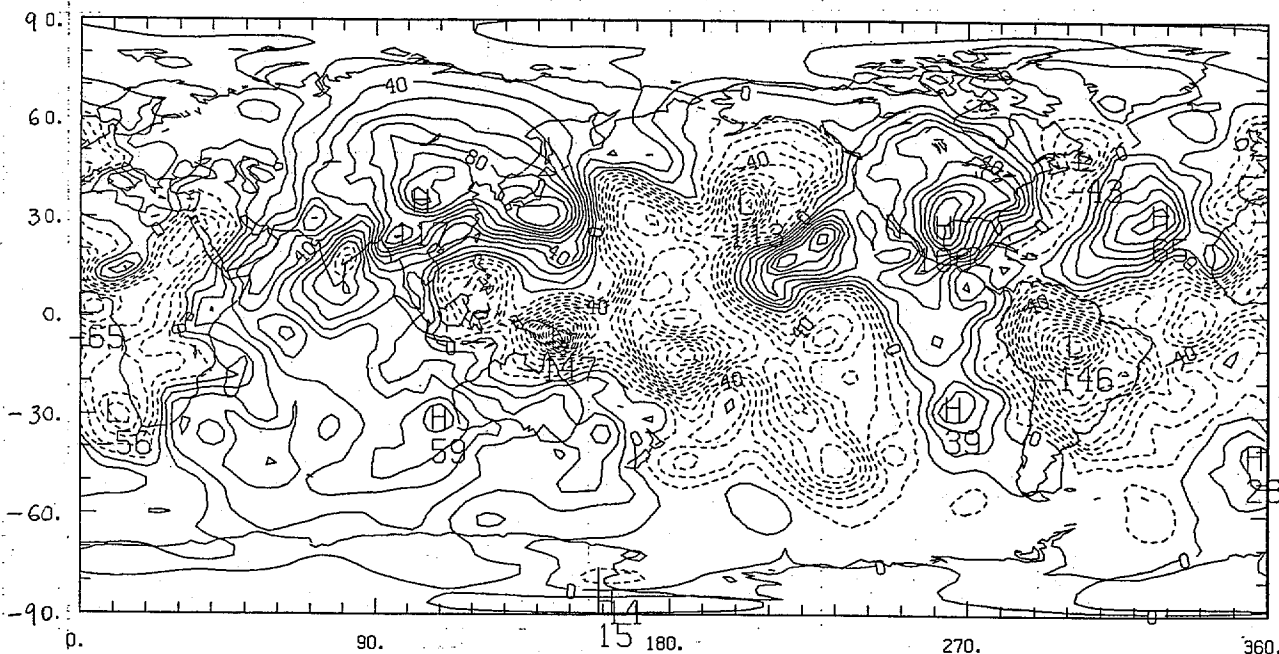
KH(12Z,AFTM) LEVEL 14 1/21/85 SIG=0.250



CONTOUR FROM -0.17000E+08 TO 0.16000E+08 CONTOUR INTERVAL OF 0.10000E+07 PT(3,3)= -0.11144E+07 LABELS SCALED BY 0.10000E-04

Fig. 9 a Blended velocity potential χ at $\sigma = 0.250$

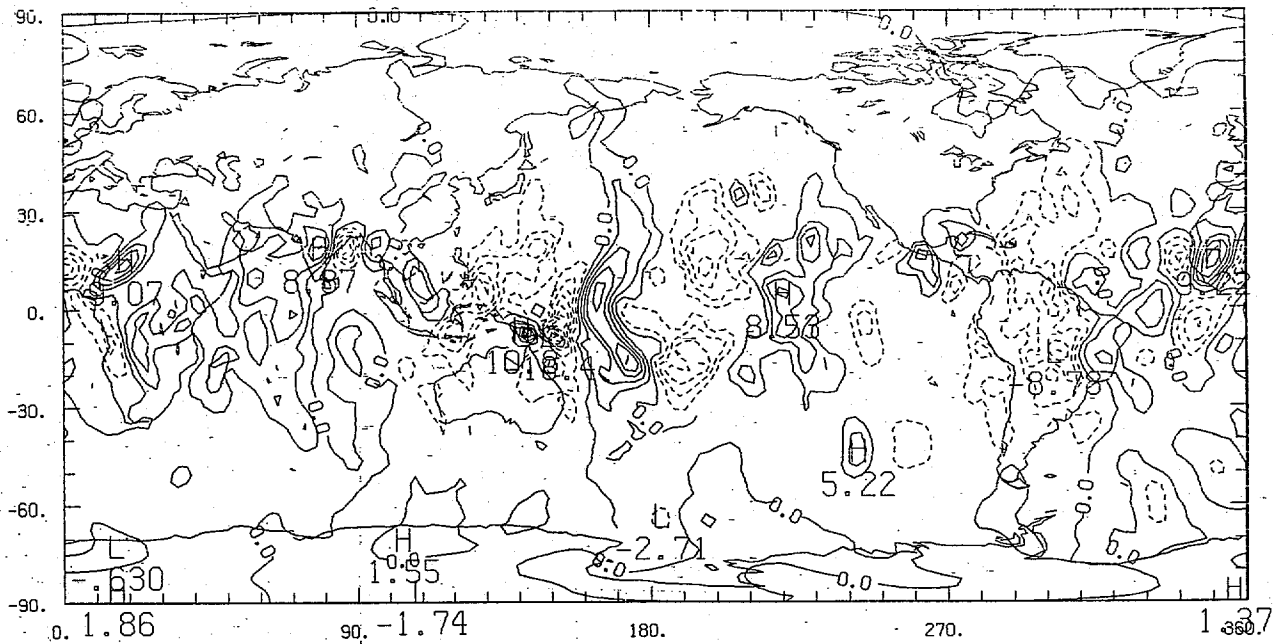
KH(12Z,ANA.) LEVEL 14 1/21/85 SIG=0.250



CONTOUR FROM -0.14000E+08 TO 0.11000E+08 CONTOUR INTERVAL OF 0.10000E+07 PT(3,3)= 0.23112E+06 LABELS SCALED BY 0.10000E-04

Fig. 9 b Analyzed velocity potential χ at $\sigma = 0.250$

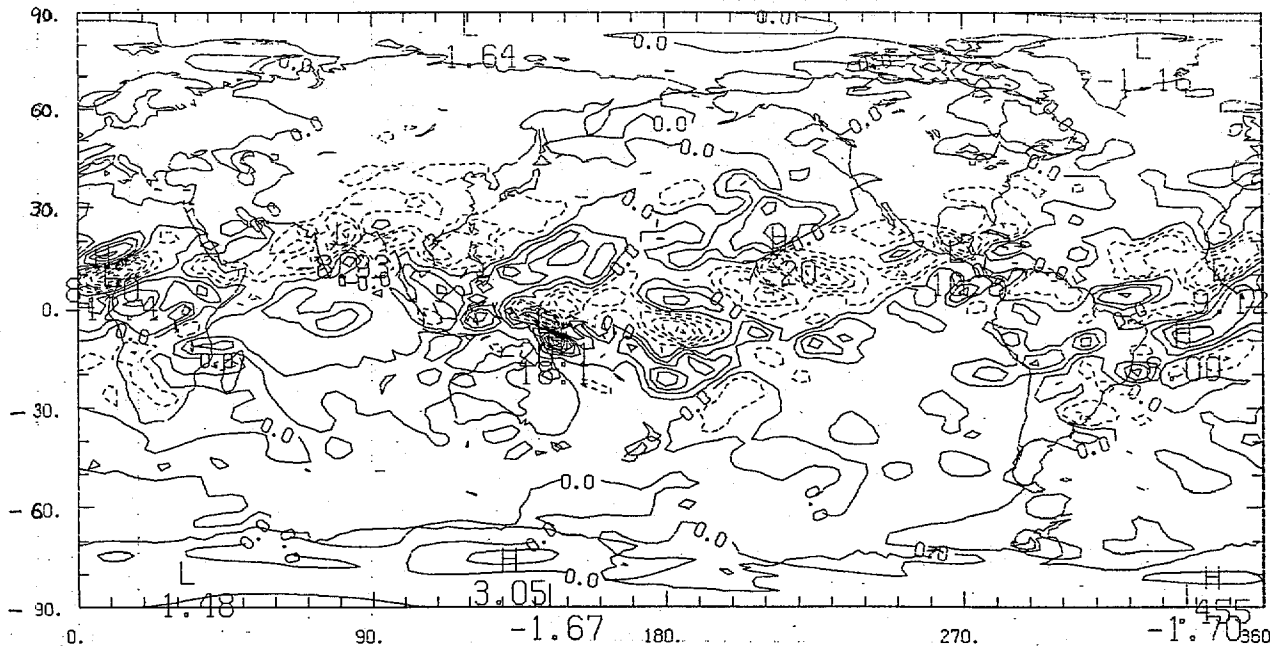
UKH(12Z,M - A) LEVEL 14 1/21/85 SIG=0.250



CONTOUR FROM -18.000 TO 10.000 CONTOUR INTERVAL OF 2.0000 PT(3,3)= 1.7396 (m sec⁻¹)

Fig. 10 a Blended - Analyzed U_D divergent velocity component. $\sigma = 0.250$

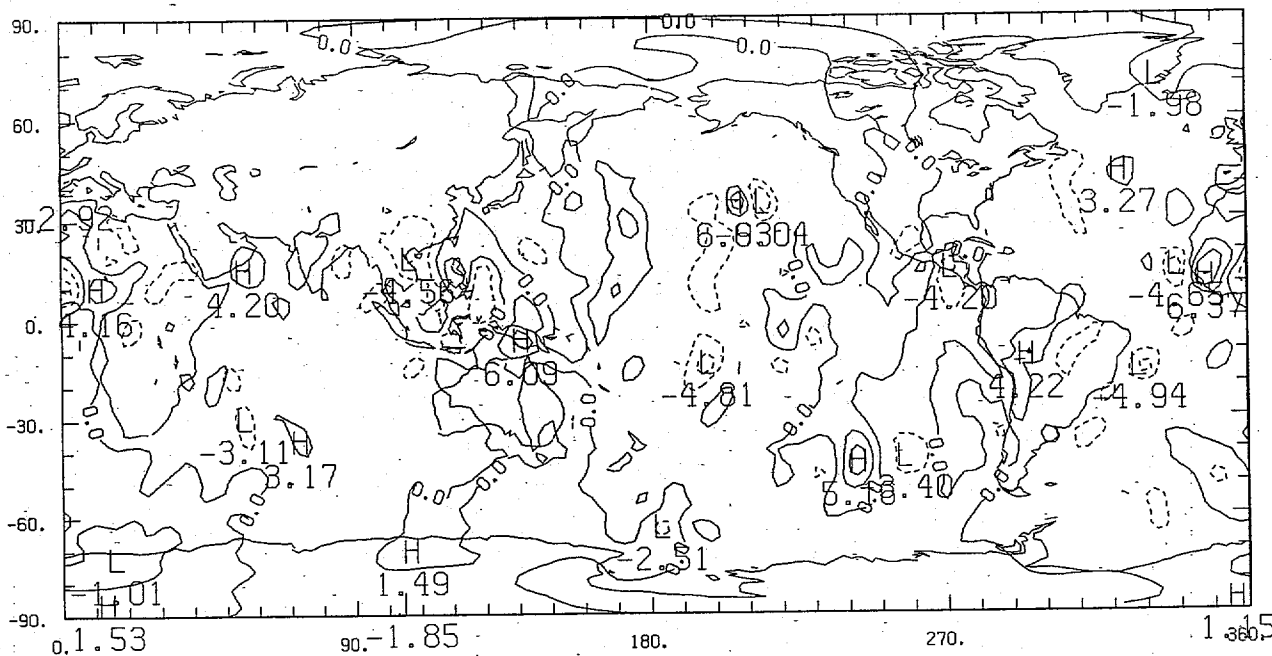
VKH(12Z,M - A) VI LEVEL 14 1/21/85 SIG=0.250



CONTOUR FROM -20.000 TO 18.000 CONTOUR INTERVAL OF 2.0000 PT(3,3)= -1.1296 (m sec⁻¹)

Fig. 10 b Blended - Analyzed V_D divergent velocity component. $\sigma = 0.250$

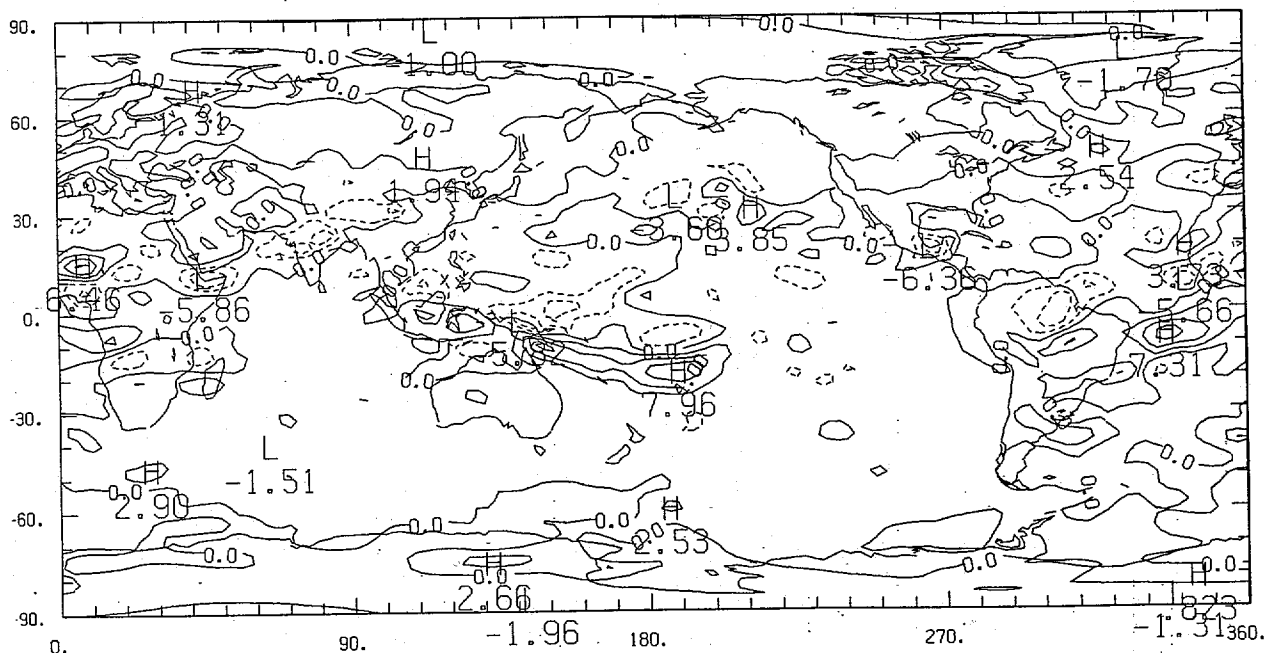
UKH(12Z,I - A) LEVEL 14 1/21/85 SIG=0.250



COUNTOUR FROM -6.0000 TO 6.0000 COUNTOUR INTERVAL OF 2.0000 PT(3,3)= 1.4453 (m sec⁻¹)

Fig. 11 a Initialized - Analyzed u_0 divergent velocity component. $\sigma = 0.250$

VKH(12Z,I - A) LEVEL 14 1/21/85 SIG=0.250



COUNTOUR FROM -6.0000 TO 6.0000 COUNTOUR INTERVAL OF 2.0000 PT(3,3)= -0.90060 (m sec⁻¹)

Fig. 11 b Initialized - Analyzed v_0 divergent velocity component. $\sigma = 0.250$

U(12Z,AFTVI) LEVEL 14 1/21/85 SIG=0.250

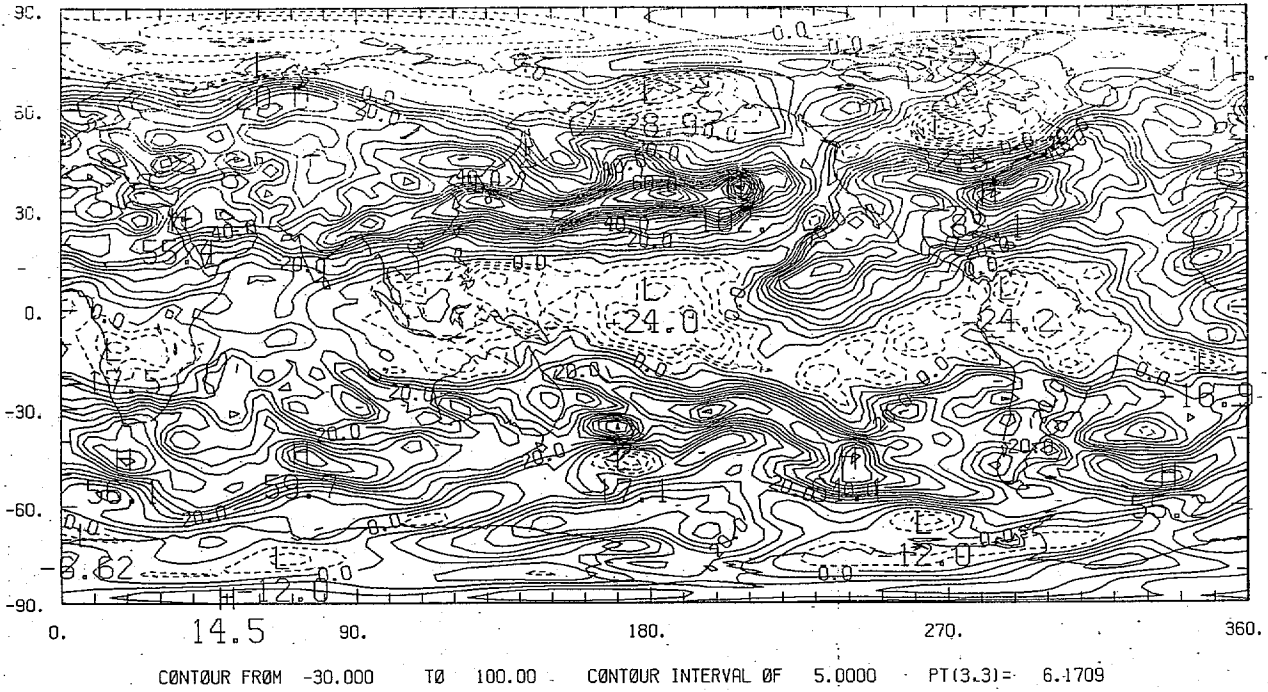


Fig. 12 a Blended total wind U component ($m sec^{-1}$). $\sigma = 0.250$

V(12Z,AFTVI) LEVEL 14 1/21/85 SIG=0.250

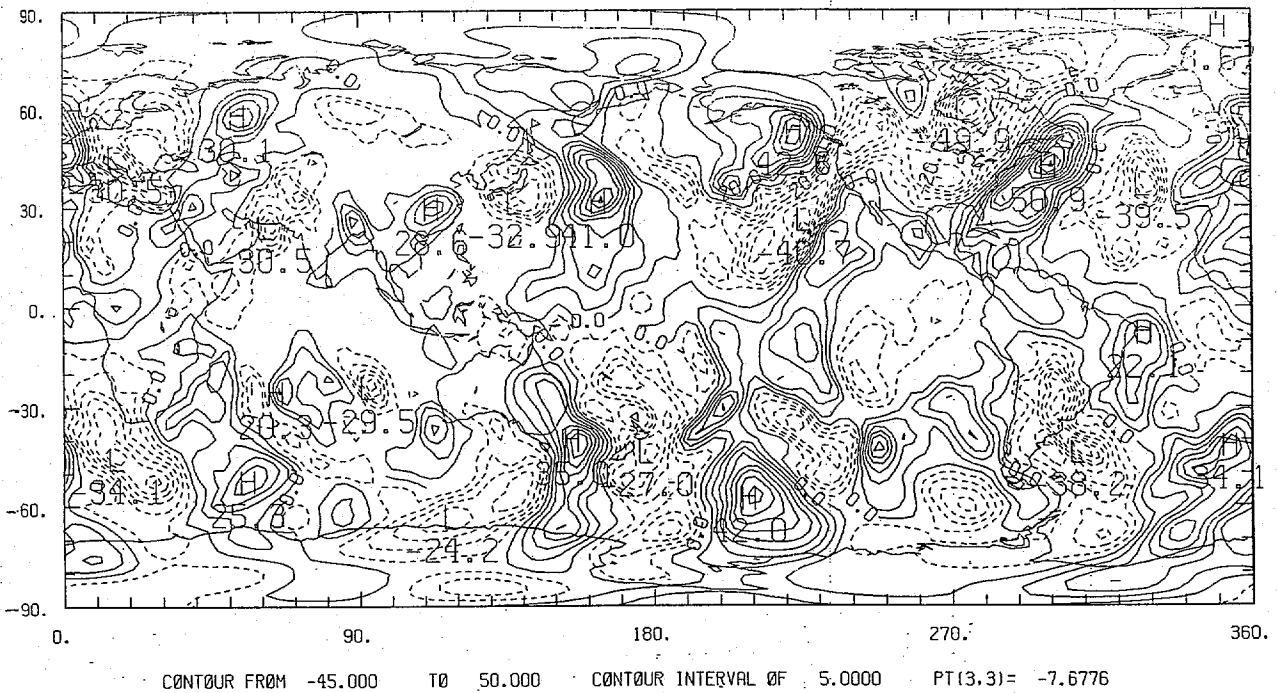
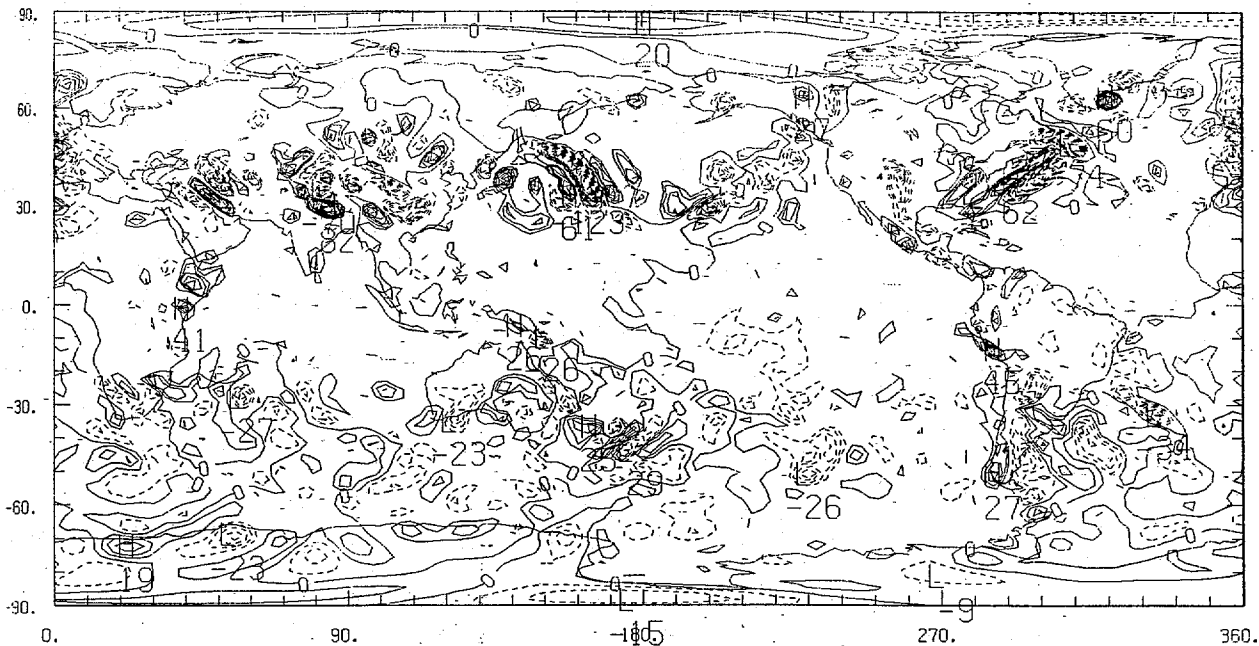


Fig. 12 b Blended total wind V component ($m sec^{-1}$). $\sigma = 0.250$

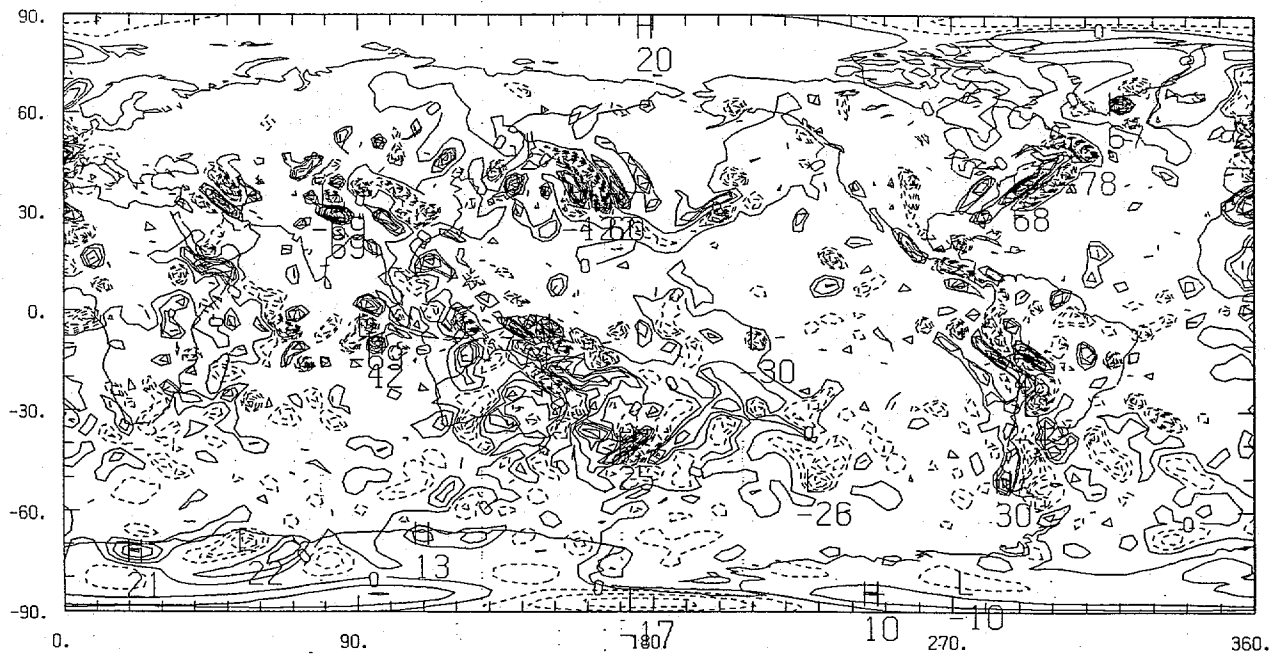
DIV(12Z,AFTVI) LEVEL 2 1/21/85 SIG=0.917



CONTOUR FROM -0.12000E-03 TO 0.75000E-04 CONTOUR INTERVAL OF 0.50000E-05 PT(3.3)= 0.11121E-05 LABELS SCALED BY 0.10000E+07

Fig. 13 a Blended divergence D at $\sigma = 0.917$

DIV(12Z,ANA.) LEVEL 2 1/21/85 SIG=0.917



CONTOUR FROM -0.12000E-03 TO 0.65000E-04 CONTOUR INTERVAL OF 0.50000E-05 PT(3.3)= 0.19430E-05 LABELS SCALED BY 0.10000E+07

Fig. 13 b Analyzed divergence D at $\sigma = 0.917$

DIVE(12Z, IN) AT LEVEL 2 1/21/85 SIG=0.917



CONTOUR FROM -0.12000E-03 TO 0.75000E-04 CONTOUR INTERVAL OF 0.50000E-05 PT(3,3)= 0.11121E-05 LABELS SCALED BY 0.10000E+07

Fig. 13 c Initialized divergence D at $\sigma = 0.917$.

UVKH(12Z,AFTVI) LEVEL 2 1/21/85 SIG=0.917

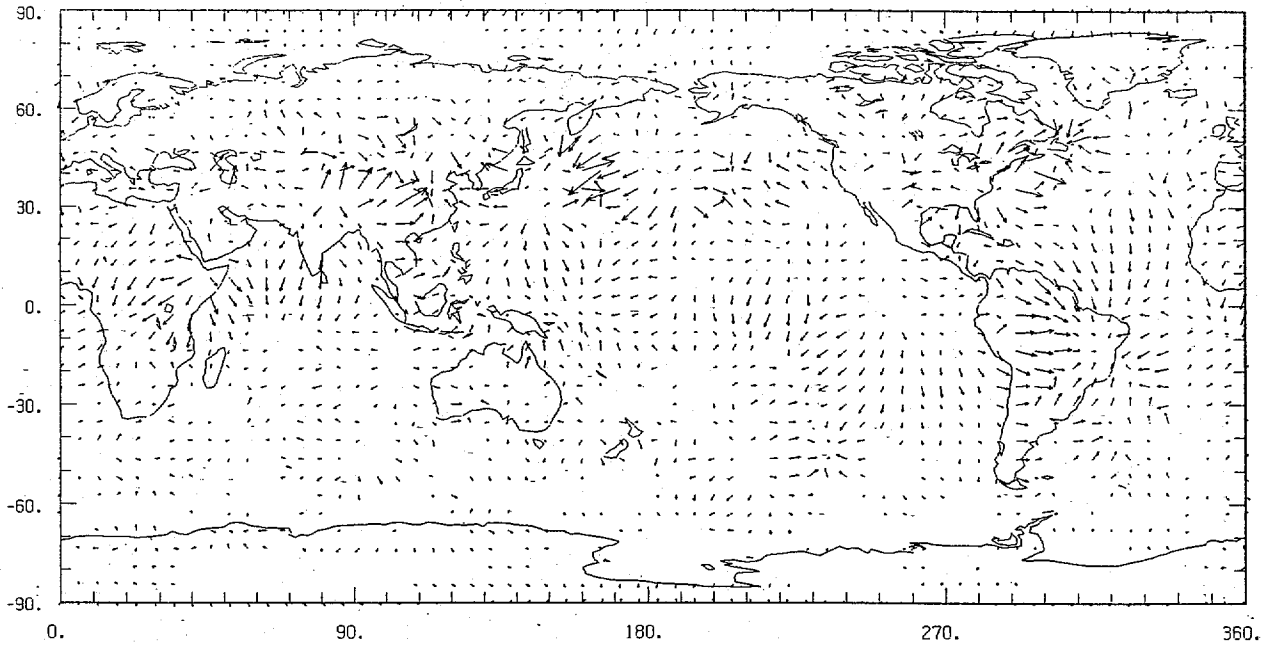


Fig. 14a. Blended divergent velocity at $\sigma = 0.917$

$m\ sec^{-1}$
0.250E+02
MAXIMUM VECTOR

UVKH(12Z,ANA.) LEVEL 2 1/21/85 SIG=0.917

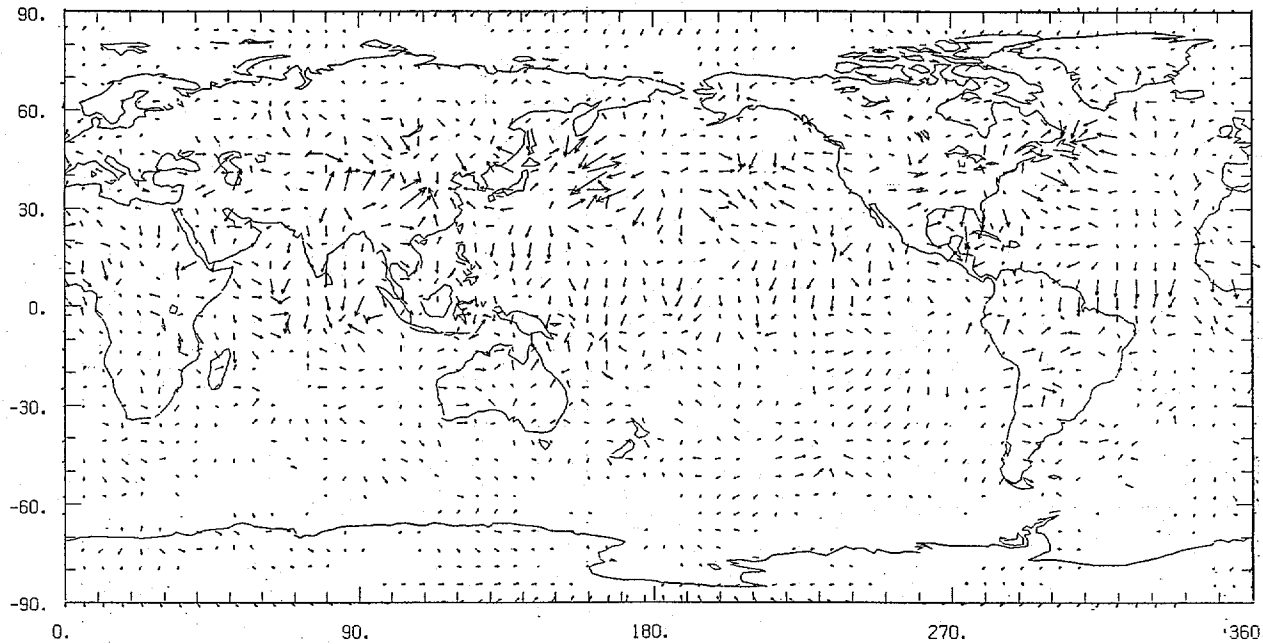


Fig. 14 b Analyzed divergent velocity at $\sigma = 0.917$

$m\ sec^{-1}$
0.250E+02
MAXIMUM VECTOR

UVKH(12Z,INI.) LEVEL 2 1/21/85 SIG=0.917

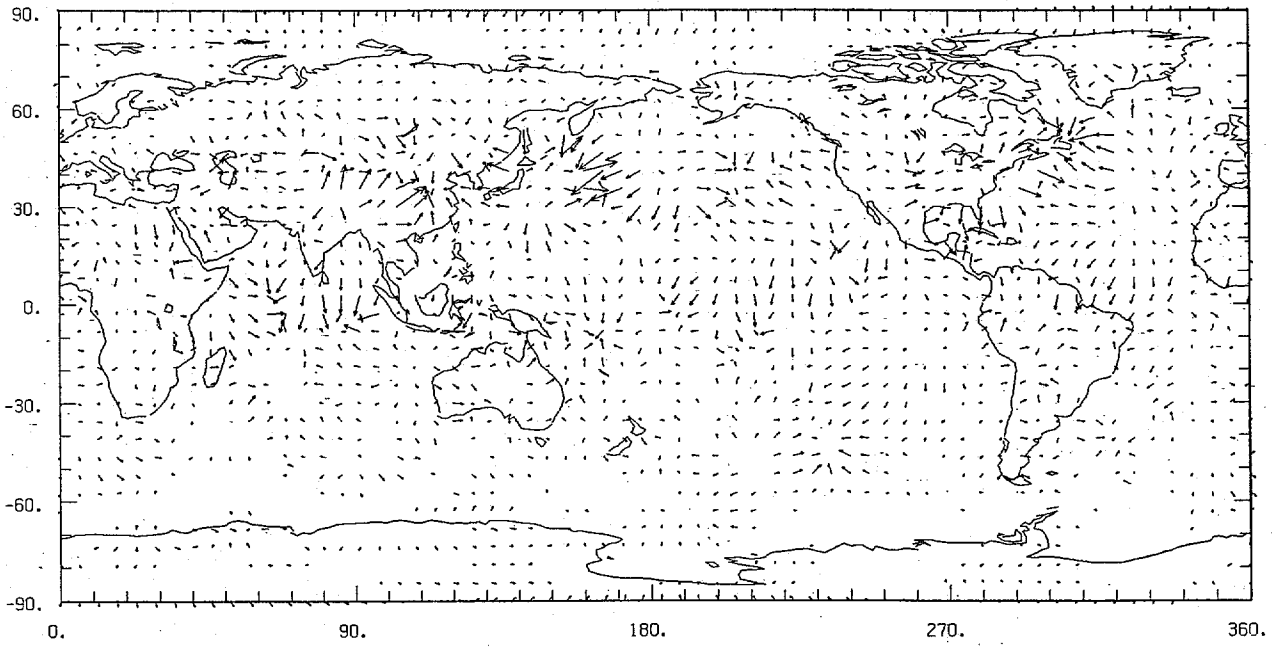
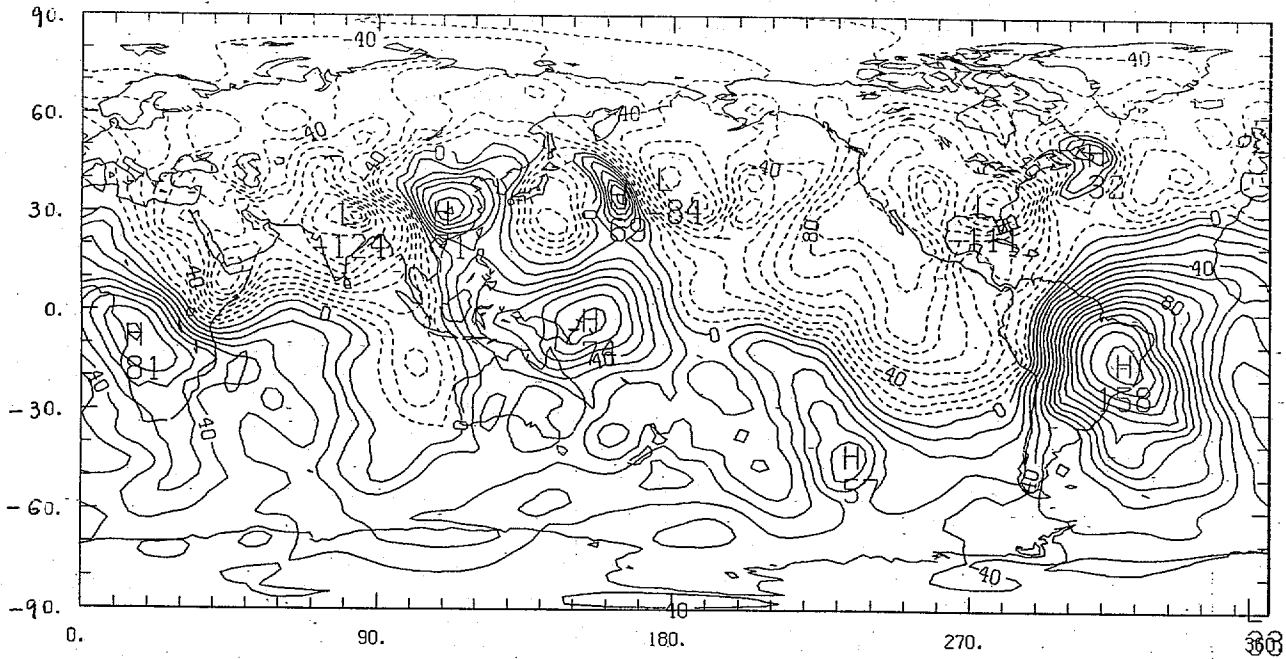


Fig. 14 c. Initialized divergent velocity at $\sigma=0.917$

0.250E+02 m sec⁻¹
MAXIMUM VECTOR

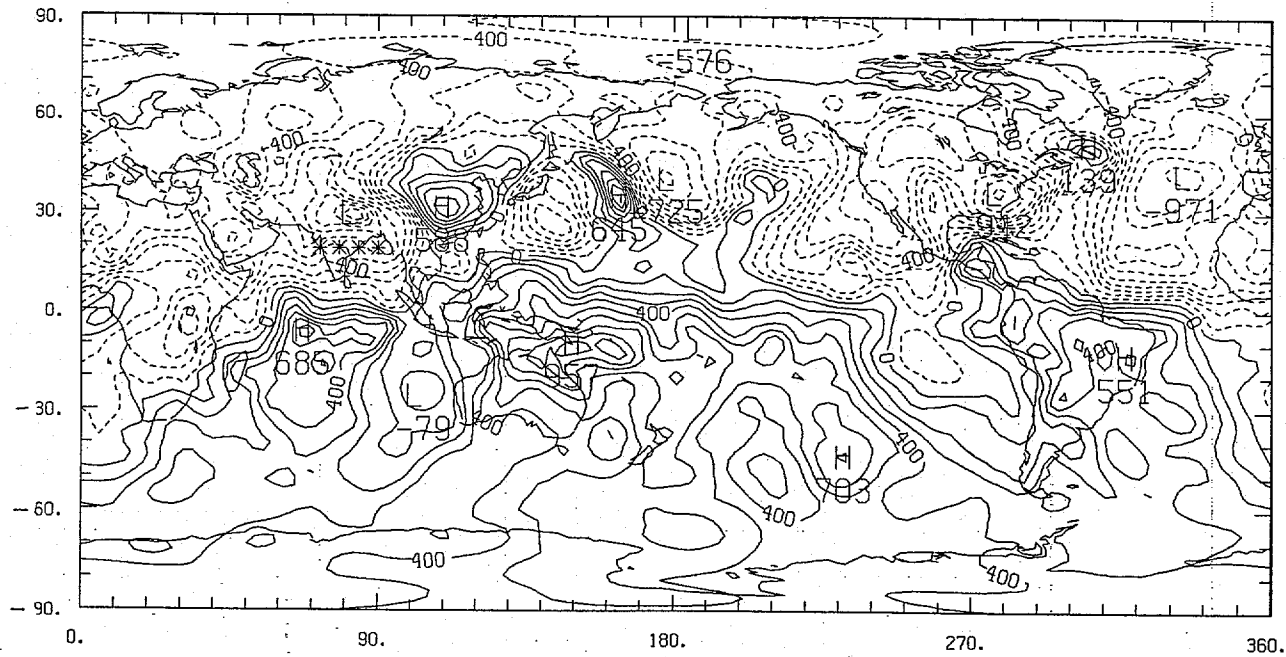
KH(12Z,AFTM) LEVEL 2 1/21/85 SIG=0.917



CONTOUR FROM -0.12000E+08 TO 0.15000E+08 CONTOUR INTERVAL OF 0.10000E+07 PT(3.3)= 0.33899E+07 LABELS SCALED BY 0.10000E-04

Fig.15 a Blended velocity potential at $\sigma=0.917$

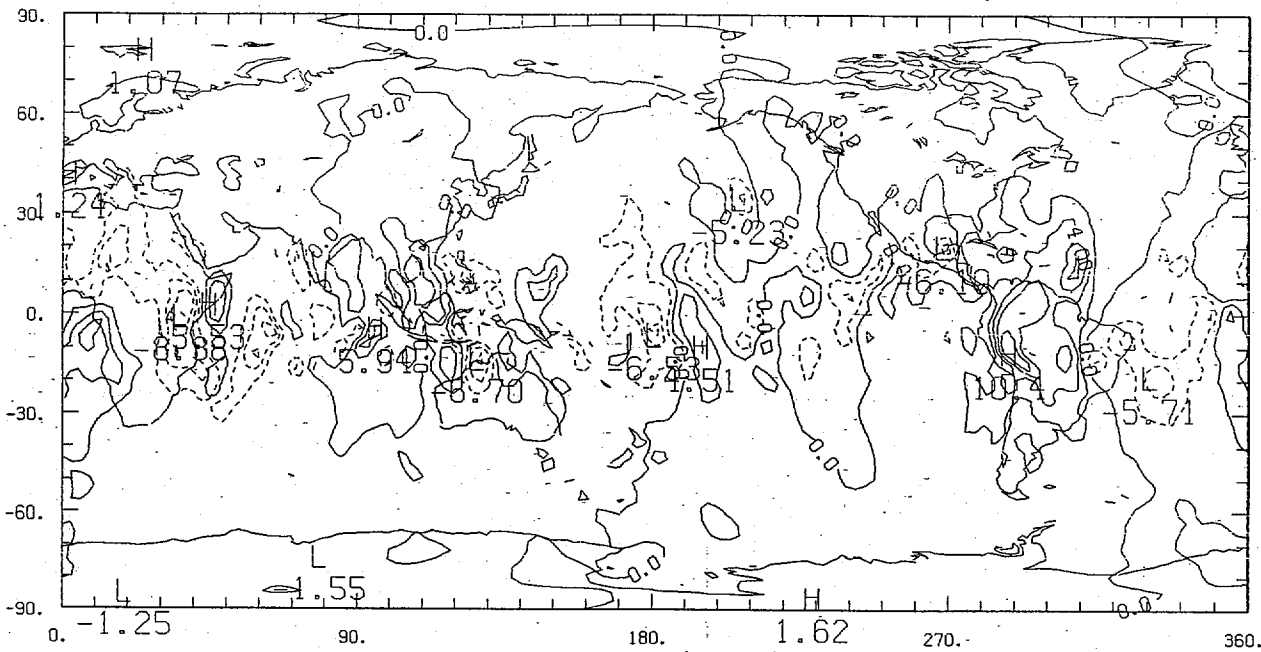
KH(12Z,ANA.) LEVEL 2 1/21/85 SIG=0.917



CONTOUR FROM -0.10000E+08 TO 0.90000E+07 CONTOUR INTERVAL OF 0.10000E+07 PT(3.3)= 0.35457E+07 LABELS SCALED BY 0.10000E-03

Fig.15 b Analyzed velocity potential at $\sigma=0.917$

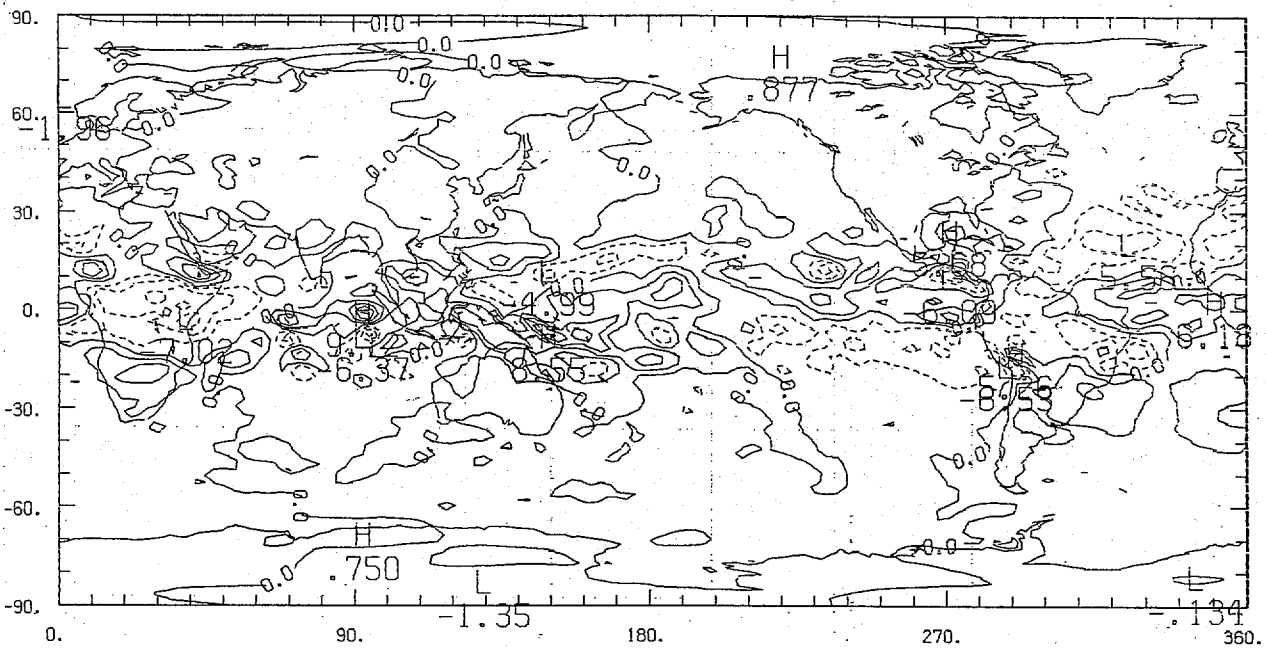
UKH(12Z,M - A) LEVEL 2 1/21/85 SIG=0.917



COUNTOUR FROM -8.0000 TO 10.0000 COUNTOUR INTERVAL OF 2.0000 PT(3,3) = -1.0479 $\sigma = 0.917$

Fig. 16 a Blended-Analyzed divergent wind u velocity component.
(m sec⁻¹)

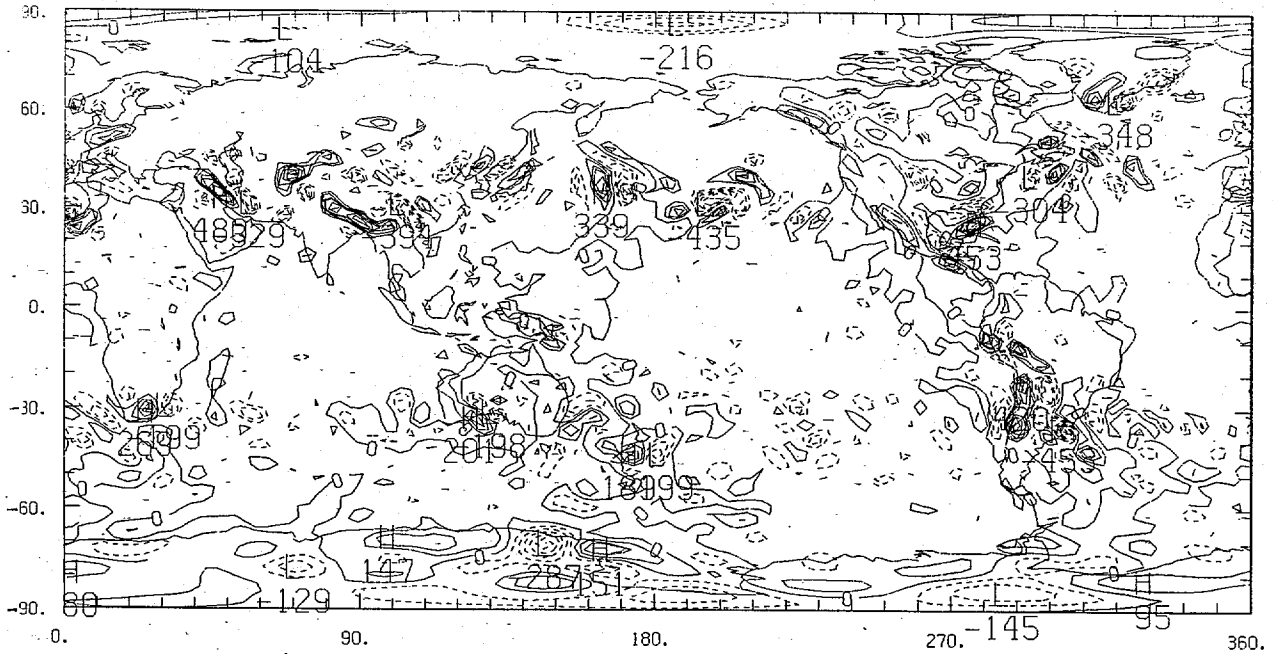
VKH(12Z,M - A) VI LEVEL 2 1/21/85 SIG=0.917



COUNTOUR FROM -6.0000 TO 8.0000 COUNTOUR INTERVAL OF 2.0000 PT(3,3) = 0.60359 $\sigma = 0.917$

Fig. 16 b Blended-Analyzed divergent wind v velocity component.
(m sec⁻¹)

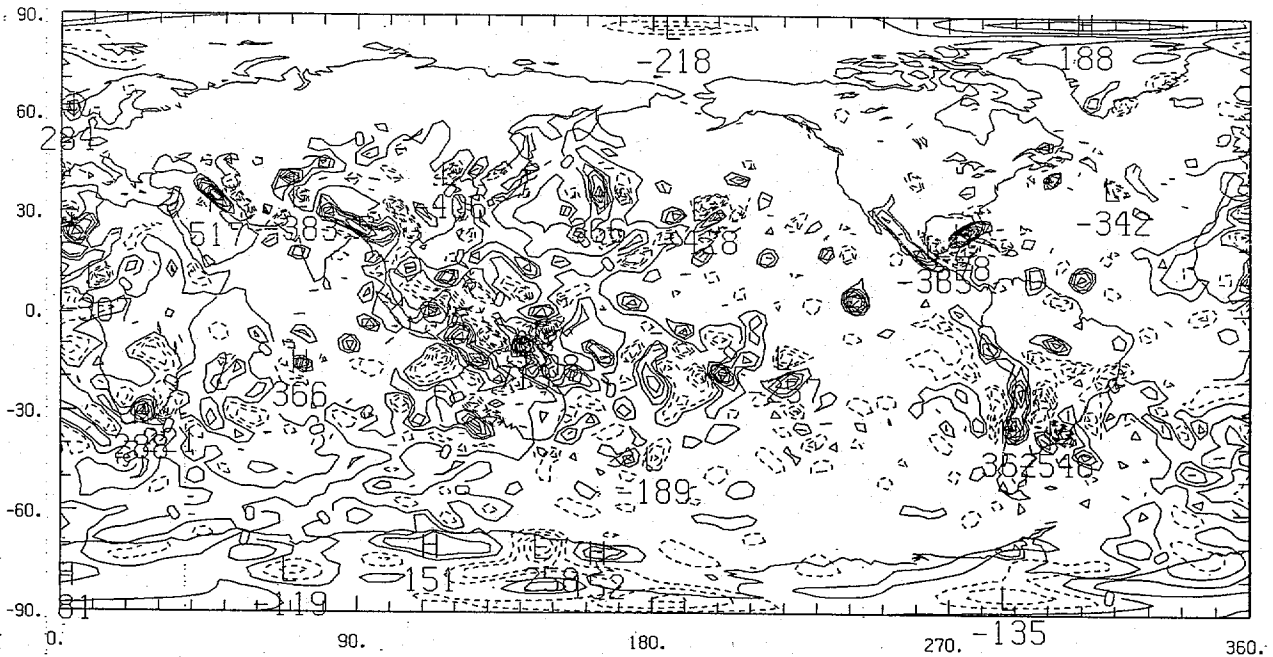
DIV(12Z,AFTVD) LEVEL 8 1/21/85 SIG=0.583



CONTUR FROM -0.45000E-04 TO 0.45000E-04 CONTUR INTERVAL OF 0.50000E-05 PT(3,3)= 0.33893E-05 LABELS SCALED BY 0.10000E+08

Fig. 18 a Blended divergence D at $\sigma = 0.583$.

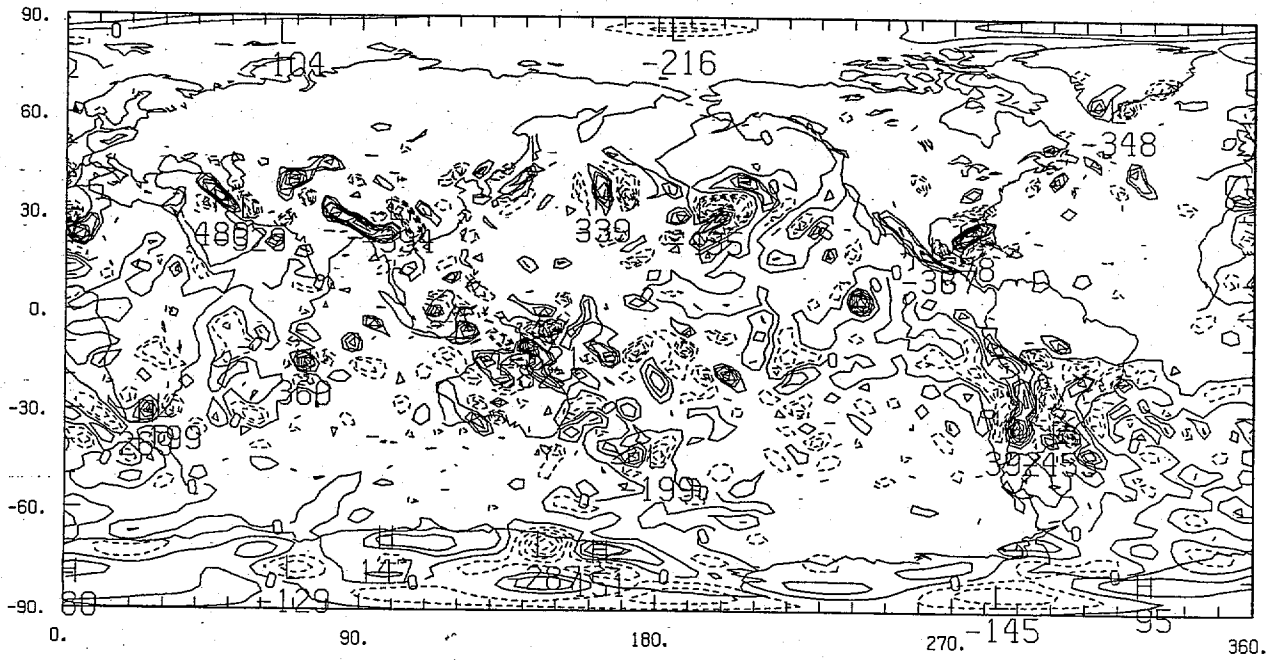
DIV(12Z,ANA.) LEVEL 8 1/21/85 SIG=0.583



CONTUR FROM -0.60000E-04 TO 0.70000E-04 CONTUR INTERVAL OF 0.50000E-05 PT(3,3)= 0.37267E-05 LABELS SCALED BY 0.10000E+08

Fig. 18 b Analyzed divergence D at $\sigma = 0.583$

DIVE(12Z,IN) AT LEVEL 8 1/21/85 SIG=0.583



C0NT0UR FR0M -0.60000E-04 T0 0.55000E-04 C0NT0UR INTERVAL 0F 0.50000E-05 PT(3.3)= 0.33893E-05 LABELS SCALED BY 0.10000E+08

Fig. 18C Initialized divergence D at $\sigma=0.583$.